A&A 486, 437–452 (2008)
DOI: 10.1051/0004-6361:200809446

Astronomy & Astrophysics

Comparing CN and CH line strengths in a homogeneous spectroscopic sample of 8 Galactic globular clusters⋆,⋆⋆

A. Kayser[1,2], M. Hilker[3,4], E. K. Grebel[1,2], and P. G. Willemsen[3]

[1] Astronomisches Institut der Universität Basel, Venusstrasse 7, 4102 Binningen, Switzerland
e-mail: andrea.kayser@unibas.ch
[2] Astronomisches Rechen-Institut, Zentrum für Astronomie, Universität Heidelberg, Mönchhofstraße 12–14, 69120 Heidelberg, Germany
[3] Argelander-Institut für Astronomie, Auf dem Hügel 71, 53121 Bonn, Germany
[4] ESO, Karl-Schwarzschild-Str. 2, 85748 Garching bei München, Germany

Received 24 January 2008 / Accepted 14 April 2008

ABSTRACT

Our work focuses on the understanding of the origin of CNO-anomalies, which have been detected in several Galactic globular clusters. The novelty and advantage of this study is that it is based on a homogeneous data set of hundreds of medium-resolution spectra of stars in eight Galactic globular clusters (M 15, M 22, M 55, NGC 288, NGC 362, NGC 5286, Palomar 12, and Terzan 7). Two of the clusters (Palomar 12 and Terzan 7) are believed to be former members of the Sagittarius dwarf spheroidal (Sgr dSph) galaxy. The large homogeneous data set allows for a detailed differential study of the line strengths in the stellar spectra of the observed clusters. Our sample comprises stars in different evolutionary states, namely the main-sequence turn-off (MSTO) region, the subgiant branch (SGB) and the base of the red giant branch (RGB). We compare the relative CN and CH line strengths of stars in the same evolutionary states (with similar log g and $T_{\rm eff}$). The majority of the examined clusters show significant variations in their CN and CH abundances at the base of the RGB. We confirm the presence of a bimodal distribution in CN for the second parameter pair of the clusters (NGC 288 and NGC 362). The two probable former Sgr dSph clusters do not exhibit any CN-strong stars. Overall, our results suggest that the environment in which the clusters formed is responsible for the existence of CN-strong stars. We can confirm the known anticorrelation between CN and CH for most of the observed clusters. Although the signal of CN absorption is weaker for the hotter stars on the MSTO and SGB, we observed the same anticorrelation in these less evolved stars for the CN-bimodal clusters. Including structural parameters taken from the literature reveals that the existence of the CN-bifurcation seems to be independent of most other cluster characteristics. In particular, we do not confirm the correlation between cluster ellipticity and number of CN-strong stars. However, there may be a trend toward an increased percentage of CN-strong stars with increasing cluster tidal radius and total luminosity. We argue that our findings are consistent with pollution by intermediate AGB stars and/or fast rotating massive stars and two generations of star formation in luminous clusters with larger tidal radii at greater Galactocentric distances.

Key words. stars: abundances – Galaxy: globular clusters: general

1. Introduction

Among the about 150 known Galactic globular clusters (GC) there exist several clusters that show star-to-star abundance variations for certain chemical elements (see review from Gratton et al. 2004). These variations are ubiquitous particularly for light elements such as C and N and are seen mainly for stars on the red giant branch (RGB). Stars with significantly stronger cyanogen (CN) bands as compared to other stars in the same cluster have been detected as early as 1971 by Osborn in M 5 and M 10 (Osborn 1971). The existence of such stars in these and many other clusters has been confirmed repeatedly (e.g., Cohen 1978; Smith & Norris 1982, 1983; Briley et al. 1989). However, the fraction of red giants showing enriched CN bands differs from cluster to cluster (Norris 1987).

Over the last three decades spectroscopic studies of the CN and CH absorption bands often revealed a bimodality in CN that is accompanied by a broadened distribution in CH. For the majority of the CN-bimodal clusters (e.g., M 2, M 3, M 5, M 13, 47 Tuc) a CN-CH anticorrelation was detected (e.g., Smith et al. 1996). Since CN is a double-metal molecule, it can be more easily observed in stars with a higher metallicity. Nevertheless, the CN-CH anticorrelation seems to be present also in the very metal-poor cluster M 15 where no clear bimodality of CN could be detected so far (Lee 2000).

Although this topic has been studied extensively in the last decades no self-consistent model has been found to satisfactorily explain the observed chemical variations. Two main scenarios are discussed as possible origins of these abundance patterns:

1) The "evolutionary mixing" scenario: in this scenario the chemical composition in the surfaces of the stars is altered due to deep mixing effects. Material from the stellar interior is dredged-up through regions of active CNO element nucleosynthesis to the upper layers of H-burning. During the H-burning phase via the CNO-cycle N is enriched at the cost of C and O. One would therefore expect a CN-CH anticorrelation if CNO-processed material is dredged up to the stellar surface. The so-called first dredge-up, however, is not able to explain the observed abundance patterns of light elements in

⋆ Based on observations obtained at the European Southern Observatory, Chile (Observing Programs 69.D-0172 and 73.D–0273).
⋆⋆ Full Table A.1 is only available in electronic form at http://www.aanda.org

RGB stars, especially for metal-poor stars that do not possess deep enough convective envelopes according to standard models (see references in Gratton et al. 2004). An additional mixing episode is needed to explain those patterns. This can either be rotation-induced mixing (e.g., Sweigart & Mengel 1979; Charbonnel 1995) or so-called "canonical extra-mixing" (Denissenkov & VandenBerg 2003). These mechanisms naturally explain the [C/Fe]–[N/Fe] anticorrelation observed in RGB stars, however will not work for stars below the RGB bump due the increased molecular weight barrier (e.g., Iben 1968). Based on low resolution spectroscopy, various studies showed that the CN-band strength is a good indicator for the [N/Fe] abundances whereas CH traces [C/Fe] (e.g., Smith et al. 1996). As a consequence, the CN bimodality and the CN–CH anticorrelation observed on the upper RGB stars of many clusters are often interpreted as a result of deep mixing that takes place in certain stars while not in other stars.

2) The "primordial" and "self-enrichment" scenarios: in both cases the abundance variations are not due to internal stellar evolutionary effects. The "primordial" scenario assumes that there exists a "primordial floor of abundance variations" (Gratton et al. 2004) that was in place when the star cluster formed (i.e., an inhomogeneously mixed molecular cloud). In the "self-enrichment" scenario the abundance variations are caused by successive generations of stars that formed within the same star cluster. Theoretical nucleosynthesis models show that the observed abundance mix can be provided either by intermediate-mass (4–5 $M_{\odot}$) asymptotic giant branch (AGB) stars (e.g., Cottrell & Da Costa 1981; Ventura et al. 2001; Denissenkov & Herwig 2003), or by fast rotating massive (20–120 $M_{\odot}$) stars (e.g., Maeder & Meynet 2006; Decressin et al. 2007). Both types of objects expel their ejecta via slow stellar winds, which is important in order to not sweep out the gas from which the second generation shall be formed. There are mainly two ways how the enriched stars got to their peculiar abundance pattern: either, the AGB ejecta mixed well with the intracluster medium out of which the second generation formed within the cluster (Cottrell & Da Costa 1981). Or, the AGB ejecta polluted the surfaces of a certain fraction of already existing stars with well-developed radiative cores (e.g., D'Antona et al. 1983; Thoul et al. 2002). The pollution scenario, however, has difficulties to explain the sharp bimodality of CN abundances and the similarity of abundance patterns of evolved as well as unevolved stars.

Lately, the evolutionary mixing scenario has been more and more challenged as correlations/anticorrelations among these elements and the range of variations of each element appear to be independent of stellar evolutionary states (with exception of enhanced depletion of C and O seen on the RGB) (e.g., Harbeck et al. 2003a). Recent spectroscopic studies near and below the main sequence turn-off (MSTO) in the GCs M 71, 47 Tuc and NGC 6752 showed that abundance variations are already present among stars that are expected to be unaffected from deep mixing mechanisms (e.g., Cohen 1999; Harbeck et al. 2003a; Briley et al. 2004). This suggests that at least some of the abundance variations observed in evolved stars were present before the stars reached the RGB, i.e. mixing can not be the only driving mechanism of the observed abundance variations.

The "self-enrichment" scenario also is strengthened by the recent findings of multiple subgiant branches (SGB) and main sequences (MS) in several massive GCs (Bedin et al. 2004; Piotto et al. 2007), which require stellar populations with distinct abundance patterns (and ages) within the clusters. Interestingly, the multiple SGBs and MSs can best be explained by a large helium enhancement in the second/third subpopulation of a cluster (D'Antona et al. 2005), which is consistent with the expected abundances of ejecta from intermediate-mass AGB stars (e.g., D'Antona et al. 2002). Actually, these AGB stars need not have been members of the same star cluster. Bekki et al. (2007) recently suggested that massive GCs might have formed in low mass dwarfs embedded in a dark matter halo. In this scenario, the second/third generation of stars then was created out of ejecta from the external "field" AGB stars. Since products of H burning are released by fast rotating massive stars in slow winds, also this class of stars may provide the He-enhancement required to explain multiple sequences observed in globular clusters.

Coming back to the overall CNO abundances, the work by Smith et al. (1996) has shown that the total [(C + N + O)/Fe] for giants in the globular clusters M 3 and M 13 is the same for both CN-strong and CN-weak stars, which would be expected from deep mixing, dredging up CNO processed material to the stellar surfaces. Thus although mixing effects are not existent in unevolved stars they seem to play a role for red giants when studying the CN and CH bands. The challenge is to disentangle the primordial contribution to the C, N abundances from the one resulting from normal evolutionary changes. On the one hand, some basic evolution of low mass population II stars is clearly a common feature in both field and cluster stars. Smith & Martell (2003) showed that halo field giants and globular cluster giants share the same pattern of declining C as a function of increasing magnitude. The same two mixing mechanisms (first dredge-up and a second mixing episode after the RGB-bump) are acting in all population II giants. On the other hand, field stars behave very differently from cluster stars as far as "heavier" light elements (namely O, Na) are concerned (Gratton et al. 2000).

If the environment in which a cluster formed (e.g., in the disk of a galaxy vs. the center of a dark matter substructure) defines the enrichment history of a cluster, the observed abundance patters would provide an indication of the origin of the cluster. In his groundbreaking work Zinn proposed that the Galactic globular cluster system consists of various sub-systems (Zinn 1985, 1993): bulge/disk (BD), old halo (OH), young halo (YH) globular clusters. He furthermore suggested that most YH clusters might have been accreted from satellite galaxies. However, the Milky Way companions have been found to show, on average, systematically lower [α/Fe] ratios than Galactic halo stars and globular clusters (e.g., Shetrone et al. 2001; Fulbright 2002; Pritzl et al. 2005; Sbordone et al. 2007). Hence the present-day dwarfs do not seem to have contributed in a significant way to the build-up of the Galactic halo and to the YH clusters.

The aim of this work is to gain further insight into the mechanism responsible for the strong CN enhancement in some stars. We therefore concentrate on regions in the color magnitude diagrams (CMDs) where stars are believed to be unaffected by mixing effects, i.e. stars on the MS, MSTO, SGB, and lower RGB. In particular, we investigate whether there is a dependence of the CN enhancement on the overall globular cluster properties and/or the sub-class they are belonging to. We investigate if CN–CH variations are different in genuine halo clusters as compared to possibly accreted globular clusters.

This article is structured as follows. Section 2 describes our data and their reduction. Section 3 explains the measurements of the CN and CH band strength and the definition of the cyanogen excess parameter. Sections 4 and 5 present the investigation of the CN/CH anticorrelation and the search for correlations

Table 1. Log of observations.

Date	Target	RA; Dec (J2000)		Exp. time
May 2002	M 55 MSTO	294.99564	–30.88307	1800 s
	M 55 SGB	294.99646	–30.88368	2160 s
	M 55 RGB	294.99559	–30.88235	480 s
July 2004	NGC 288 MSTO	13.23313	–26.57845	5140 s
	NGC 288 SGB	13.23630	–26.57807	2700 s
	NGC 362 MSTO	15.67363	–70.84870	5400 s
	NGC 362 SGB	15.67209	–70.84886	2800 s
	NGC 5286 SGB	206.54375	–51.37364	2700 s
	M 22 MS	279.04539	–23.90313	5400 s
	M 22 SGB	279.04539	–23.90311	3000 s
	Ter 7 SGB	289.43484	–34.65680	5400 s
	Ter 7 RGB	289.43488	–34.65773	4500 s
	M 15 SGB	322.54426	12.16722	2400 s
	Pal 12 RGB	326.66087	–21.25134	2400 s

Table 2. Reddening, distance modulus, and photometric parameters of the MSTO for our sample GCs.

Cluster	E^a_{B-V}	$(m-M)^a_V$	$V_{\rm MSTO}$	$(B-V)_{\rm MSTO}$
NGC 288	0.03	14.83	18.90[b]	0.46[b]
NGC 362	0.05	14.81	similar to NGC 288[c]	
NGC 5286	0.24	15.95	20.05[d]	0.73[d]
M 22	0.34	13.60	17.70[e]	0.75[e]
Ter 7	0.07	17.05	20.96[f]	0.52[f]
M 55	0.08	13.87	17.89[g]	0.50[g]
M 15	0.10	15.37	0.50[h]	19.40[h]
Pal 12	0.02	16.47	∼20.5[i]	0.452[i]

[a] Harris (1996); [b] Alcaino et al. (1997); [c] Bellazzini et al. (2001); [d] Samus et al. (1995a); [e] Samus et al. (1995b); [f] Buonanno et al. (1995); [g] Alcaino et al. (1992); [h] Durrell & Harris (1993); [i] Stetson et al. (1989).

between other cluster properties and the number ratio of CN-strong/CN-weak stars. The final Sect. 6 gives our summary and conclusions.

2. Observations and data reduction

The spectroscopic data were obtained in May 2002 and July 2004 at the VLT/UT4 at ESO/Paranal (Chile) with the multi-slit spectroscopy instrument FORS2/MXU. FORS2 provides a field of view of 6.′8 × 6.′8. The observations of M 55 were obtained in 2002 and were also used for calibration purposes in a study of ω Cen (Hilker et al. 2004; Willemsen et al. 2005; Kayser et al. 2006). The observations obtained in 2004 were dedicated to CN and CH measurements in seven further Galactic globular clusters (M 15, M 22, M 55, NGC 288, NGC 362, NGC 5286, Palomar 12, and Terzan 7) spanning a large range in metallicity ($-2.26 < [{\rm Fe/H}] < -0.58$ dex). Two of the clusters (Palomar 12 and Terzan 7) are suggested to have originated from the Sagittarius dwarf spheroidal (Sgr dSph) galaxy (Bellazzini et al. 2003; Sbordone et al. 2005).

For both observing runs, the candidate stars for the spectroscopy were selected from pre-images in Johnson B and V. We selected target stars from the upper MS, the SGB, and the lower RGB in the cluster CMDs. On the RGB we focused on stars fainter than the RGB bump, the point where deep mixing is believed to set in (Sweigart & Mengel 1979; Charbonnel 1995).

We chose the grating with the ESO denotation 660I+25 (second order) with a dispersion of 0.58 Å pix^{-1}. The spectral region covers ∼3700 to 5800 Å including the CN band at 3885 Å and the G-band at 4300 Å. The final actual wavelength coverage depends on the location of the star/slit on the mask with respect to the dispersion direction. Typically we defined one slit mask per region of the CMD per cluster, containing ∼50–70 slits. We selected slit lengths of 4–8″ to make local sky subtraction possible. The slit width was fixed to 1.″0. The total exposure time per mask varied between 360 and 5400 s depending on the cluster and the brightness of the target stars. To facilitate cosmic ray removal the observations were split into multiple (2–3) exposures. The central coordinates of the observed fields as well as the total exposure times are listed in Table 1. In addition to the science exposures, we obtained bias, flatfield and wavelength calibration observations.

The photometric data are based on the pre-image observations of the target fields in the B and V band, taken several months prior to the spectroscopic observations with FORS2 at the VLT/UT4. The identification and psf-photometry was performed on the pipeline reduced images (provided by ESO) using the the `IRAF` package `DAOPHOT`. B and V magnitudes were matched to create the CMDs. For this work, a precise photometric calibration is not necessary since we are mainly interested in a comparative study of stars in different evolutionary states, which can easily be identified in the CMDs. A rough calibration was done by adjusting the zeropoints such that the MSTO $(B-V)$ colors and V magnitudes taken from the literature were matched (see Table 2).

Based on the location in the CMDs we assigned stars to the MS, SGB, and RGB. Figure 2 shows the CMDs for all clusters in our sample. The stars with available spectra are symbol-coded according to their position in the CMD. Only those stars are shown that were identified as radial velocity members and that passed our quality check of the spectra. For the two Sgr clusters Ter 7 and Pal 12 some stars near the RGB bump have been observed. These stars are included in the Figs. 2–4 but neglected in the further analysis.

The data reduction was carried out using standard routines within `IRAF`[1]. This included bias correction and flatfielding. The cleaning for cosmic rays was done with `bclean` from the `STARLINK` package. Before sky subtraction was performed the spectra from the individual exposures were stacked to improve the signal-to-noise ratio. In most cases, object and sky could be extracted from the same slit. The wavelength calibration was achieved using the emission spectra of the He-Ne-Hg-Cd arc lamps taken after each set of observations. Note that the final spectra were neither flux-calibrated nor normalized by the continuum. All spectra were binned to a spectral scale of 1 Å pix^{-1}. Considering the seeing the final spectral resolution (FWHM) for narrow lines is ∼2 Å. Typical spectra of a RGB, a SGB and a MS stars in NGC 288 are shown in Fig. 1.

For all spectra we measured radial velocities by cross-correlating them with five high quality template spectra taken from the ω Cen dataset using `IRAF/fxcor`. We adopted the mean value of the five measurements as the radial velocity of the star and corrected for the measured Doppler shift. The scatter of the velocity measurements is of the order of 20 km s^{-1}, which reflects the uncertainties given by the spectral resolution. In the resulting velocity distributions the globular clusters clearly stand out against the Galactic foreground. Possible non cluster member stars were identified by their radial velocities and

[1] IRAF is distributed by the National Optical Astronomy Observatories, which are operated by the Association of Universities for Research in Astronomy, Inc., under cooperative agreement with the National Science Foundation.

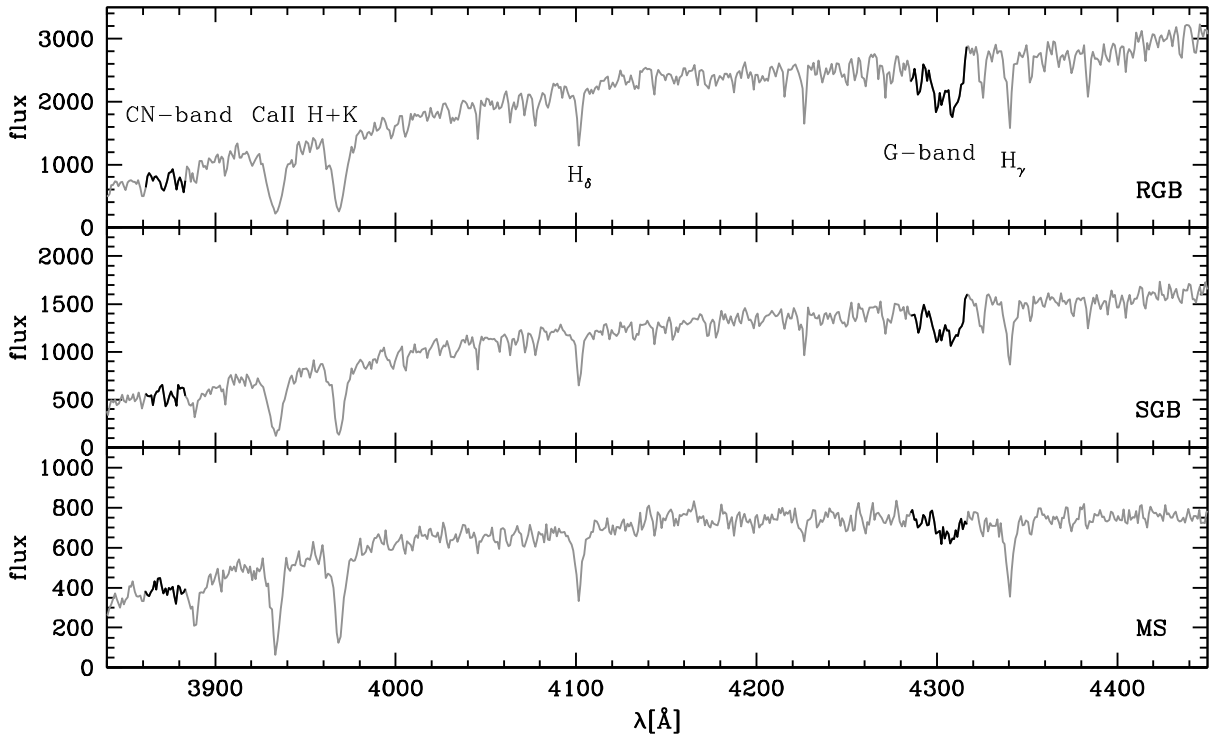

Fig. 1. Typical spectrum of a RGB (*top panel*), a SGB (*middle panel*), and a MS (*bottom panel*) star in the globular cluster NGC 288. The regions of the measured indices are marked by darker lines. Furthermore the positions of the prominent CaII H and K and Hydrogen lines are indicated *in the top panel*.

rejected from the further analysis. In a final step, we examined each spectrum individually and rejected those spectra with bad quality (e.g., due to tracing errors). In total about 500 spectra are suitable for our analysis, whereof 120 spectra are from lower RGB stars.

Note that NGC 5286 and M 22 have quite a high foreground extinction, and probably differential reddening is broadening the giant branches (e.g., Richter et al. 1999). Most of the radial velocity members of NGC 5286 lie on the red side of the RGB sequence which might reflect their biased location west of the cluster center (pointing of the spectroscopic mask).

In the Appendix, magnitude limited samples of cluster member stars that were used for our analysis are presented (Table A.1). Only the brightest five stars of each cluster are contained in this table. The full table of all cluster stars only is available in the online version of the article.

3. CN and CH band strengths

For all spectra, we measured line indices covering the absorption features of the CN and CH molecules. For the CN and CH band strengths, we used the modified S3839 and CH4300 indices as defined by Harbeck et al. (2003a):

$$S\,3839\,(\mathrm{CN}) = -2.5\ \log \frac{F_{3861-3884}}{F_{3894-3910}}, \quad (1)$$

$$\mathrm{CH4300} = -2.5\ \log \frac{F_{4285-4315}}{0.5F_{4240-4280} + 0.5F_{4390-4460}}, \quad (2)$$

where F_λ are the fluxes in the different bandpass regions. Our error estimates assume Poisson statistics in the flux measurements.

3.1. CN band strength

In order to investigate the behavior of the strengths of the CN index as a function of evolutionary state (or stellar mass) we plotted CN against the absolute V magnitude, M_V, for all clusters (Fig. 3). We adopted the distance moduli and extinction values of Harris (1996).

Looking at the whole sample of stars a wide spread in CN and a continuous increase of CN with decreasing M_V can be seen in the upper panel of this figure. This is caused by the fact that the formation of molecules in stellar atmospheres strongly depends on the effective temperature, $T_{\rm eff}$, and the surface gravity, $\log g$ of the stars. The efficiency of CN formation is higher in stars with lower $T_{\rm eff}$ and lower $\log g$. To further illustrate this effect we subdivided our sample into MS ($\log g \sim 4.5$, $T_{\rm eff} \sim 6000$ K), SGB ($\log g \sim 4.5$–3, $T_{\rm eff} \sim 5000$–6000 K), and RGB stars ($\log g \sim 3$, $T_{\rm eff} \sim 5000$ K). The different distributions for the different evolutionary states are shown in the lower panels. One can clearly see that the line strengths of CN on average increase as stars evolve from the MS to the RGB. This can be understood by the augmented formation of molecules in cooler atmospheres.

Looking at the globular clusters individually one recognizes that they show very different behaviors in the M_V vs. CN diagram. Whereas for the MS and the SGB all clusters show roughly the same pattern, the distributions on the RGB deviate between the clusters. For some clusters like e.g., NGC 288 and NGC 362, we clearly see a bifurcation in CN band strengths as we reach the RGB. Either part of the bifurcation contains roughly equal numbers of stars. This is worth to keep in mind as the two clusters are a so called "second-parameter pair": both clusters have similar metallicities but show a very distinct horizontal branch morphology. In NGC 288, most of the core helium

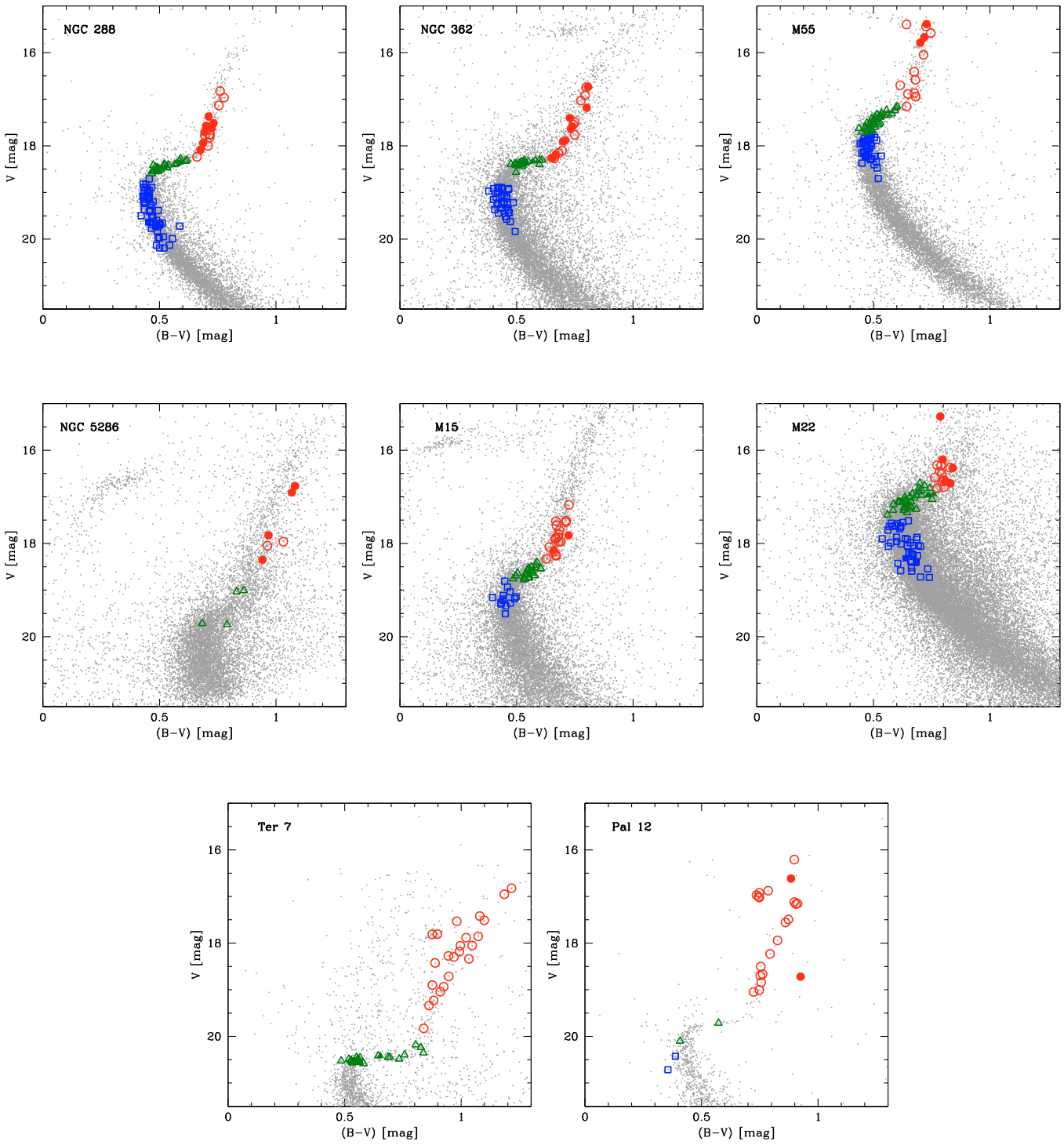

Fig. 2. The color magnitude diagrams for the globular clusters in our sample. Those stars for which line strength measurements are available are marked in color. We distinguish between stars of different evolutionary states. MS stars are indicated by blue squares, SGB stars by green triangles, and RGB stars by red circles. CN-weak and CN-strong stars are denoted by open and filled symbols, respectively. Note that in all diagrams the calibrated pre-image B and V magnitudes are shown. Our sample comprises clusters spanning a wide range in metallicity ($-2.26 <$ [Fe/H] < -0.58 dex). The clusters Palomar 12 and Terzan 7 are believed to be part of the Sgr dSph, which is currently being disrupted by its tidal interaction with the Milky Way.

burning stars can be found on the blue horizontal branch whereas almost no stars are located on the red part. Exactly the opposite is the case for NGC 362. For this cluster the red part of the horizontal branch is densely populated. Some authors proposed that deep mixing and the consequently increased mass loss could be an explanation for the different horizontal branch morphologies as well as the observed abundance anomalies (e.g., Weiss et al. 2000). For other second parameter pairs like e.g., M 3 and M 13,

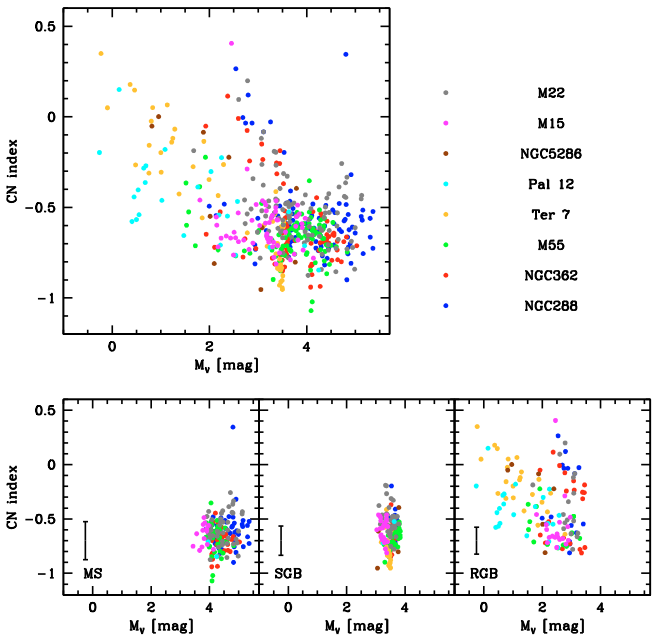

Fig. 3. The distribution of the stars of the different clusters in the CN vs. M_V diagram. *The left upper panel* illustrates the overall distribution of our sample stars. In *the lower panel* we distinguished between different evolutionary states of the stars. The color coding of the data points corresponds to stars from the different clusters as indicated in the figure legend in *the upper right*. Whereas for the MS all clusters show roughly the same distribution, for the RGB the distribution shows a large scatter. For the clusters NGC 288 and NGC 362, a bimodal distribution in CN band strength is visible. In the lower left corner of *the bottom panels* the median errors of the measurements are shown.

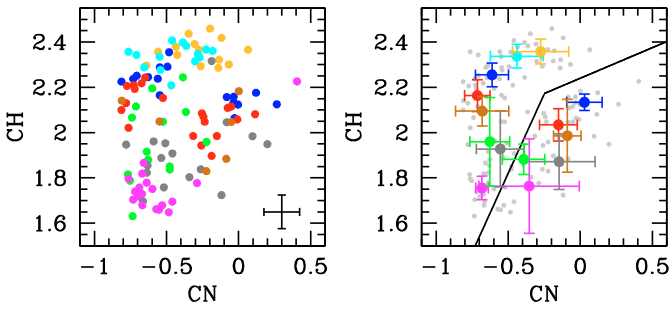

Fig. 4. The distribution of the stars in the CN vs. CH diagram for the RGB star in our sample clusters. The stars of different clusters are indicated by different colors as listed in Fig. 3. *The left panel* illustrates the overall distribution of our sample stars, with a typical error given in the lower right corner. The solid line indicated a possible differentiation between CN-strong and CN-weak stars in this diagram, drawn by eye. *In right panel* we calculated the mean CN and CH of both the CN-strong and CN-weak stars. The original overall distribution is plotted in gray, while the mean values are color-coded as defined before.

which also show differences in light abundance elements this might be a possible explanation for the observed patterns. Both clusters have similar ages and metallicities. However, the RGB in M 3 is dominated by CN-weak stars, whereas the majority of stars in M 13 are found to be CN-strong (e.g., Suntzeff 1981).

Nevertheless, the fact that we do not observe significant differences in the CN distributions indicates that deep mixing cannot be a major cause of the horizontal branch morphology. Similarly, based on the CN and CH measurements of stars in the second parameter globular cluster NGC 7006, Harbeck et al. (2003b) argued against the hypothesis that CN-variations are directly correlated with the second parameter effect. They found the scatter in CN to be similar to those in other GCs of the same metallicity but different horizontal branch ratios.

In contrast to NGC 288 and NGC 362, the clusters Ter 7, Pal 12, and M 55 seem to exhibit no or only very few stars with strong CN band strengths. In the clusters NGC 5286, M 22, and M 15, stars can be found on both the CN-weak and the CN-strong regime in this diagram. For M 15 and M 22, the majority of the stars are associated with the CN-weak group. For NGC 5286, we have only six measurements. Four of these stars are found to be CN-strong and two CN-weak.

We cannot assess whether similar abundance variations on the SGB and the MS region are not present or can not be detected due to a too weak signal caused by the higher effective temperatures of these stars. The observed scatter in the CN measurements of MS and SGB stars (rms ~ 0.13 and 0.14, respectively) is found to be of the same order as the errors in the index measurements (0.17 and 0.13, respectively).

CN as a double-metal molecule is easier to observe in more metal-rich clusters due to the stronger equivalent widths at higher metallicities. Our work as well as former studies on the RGB show that whatever process is responsible for the formation of the CN-strong stars, it seems to occur in the majority of Galactic globular clusters. In contrast to this, in both fairly metal-rich Sgr dSph clusters (Pal 12 and Ter 7) we found no sign for this process to be present. All stars in these clusters are located in the CN-weak branch in Fig. 3. From the fact that, if present, CN-strong stars should show up easily in these clusters we infer that they actually lack those stars. This suggests that probably the environment in which the clusters formed had an effect on the presence or absence of the CN variations. However we point out that possible effects of the small sample size cannot be ruled out. Preliminary results from low resolution spectra of seven giants in Arp 2 and Ter 7 suggest star to star variations in the CN band strength in these clusters (Briley et al. 2007).

3.2. CN vs. CH

The CN vs. CH diagram also allows us to study CN bimodalities. In Fig. 4 (left panel) we plot the measured CN vs. the CH band strengths for the RGB stars in our sample clusters. The overall patterns found for RGB stars in Fig. 3 also show up in Fig. 4. A clear bifurcation into two branches is detected in the CN vs. CH diagram for stars on the RGB. NGC 288 and NGC 362 show the strong bimodality in the distribution of CN line strength, seen before. In contrast, the RGB data points of Ter 7 and Pal 12 again are both located on the CN-weak branch in Fig. 4. Due to their fairly high metallicities these clusters are found in the CH-strong regime in this diagram. It seems as if the two Sgr clusters are more homogeneous in their CN abundances than the Galactic globular clusters in our sample.

Interestingly, the stars in M 15, which showed no indication for a bifurcation in Fig. 3, show a weak indication of a bimodal distribution (two clumps separated at CN ~ −0.6) in the CN-CH plane (Fig. 4). However, this needs further confirmation since the observational errors of such weak lines are large compared to the separation of the two clumps. Assuming that the clump at CN = −0.5 and CH = 1.65 defines the CN-rich population, this would strongly change the number ratio of CN-strong to CN-weak stars in M 15 (see next section). In order to

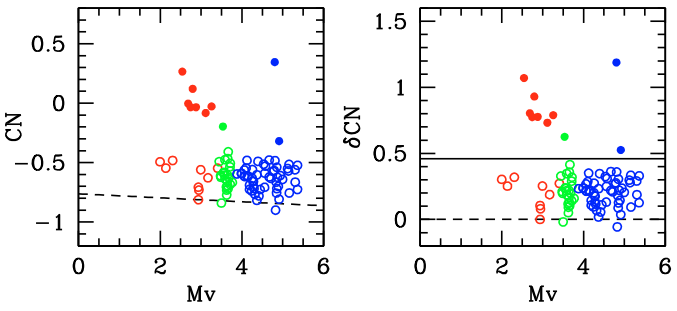

Fig. 5. *Left*: the M_V vs. CN diagram for the RGB (red), SGB (green), and MS (blue) stars for the cluster NGC 288. The bimodal distribution is clearly visible. The dashed line illustrates the lower envelope fitted to this distribution. *Right*: plotted is M_V vs. the CN excess parameter δCN. Stars with δCN > 0.46 are defined as CN-strong and indicated by filled circles. CN-weak stars are indicated by open circles. The solid line indicates the separation between CN-strong and CN-weak stars.

further illustrate the dichotomy in this plot we separated CN-strong from CN-weak stars (see Fig. 4 right panel) and calculated the mean CN- and CH-indices for each sub-population in the different clusters (large dots).

As we introduced earlier, one of the scenarios proposed to explain the variations in C and N in RGB stars in globular clusters is the dredge-up of material processed in the CNO cycle. In our case, the origin of the observed patterns/bimodalities can not only lie in such mixing effects as the analyzed stars are considerably fainter than the red bump at which the deep mixing mechanism is expected to set in. Although we did not find evidence for CN bimodalities among our SGB and MS stars (cf. Harbeck et al. 2003a) we favor a scenario in which the cluster formed out of chemically inhomogeneous material that was polluted by the outflows of fast rotating massive stars or AGB stars (e.g., Cottrell & Da Costa 1981; Ventura et al. 2001; Decressin et al. 2007).

3.3. Cyanogen excess parameter (δCN)

As a measure to quantify the wide range of CN line strengths we used a CN excess parameter (δCN) similar to the one introduced by Norris & Smith (1981). This minimizes the effects of effective temperature and surface gravity existent in the CN measurements. The δCN parameter is defined as the CN strength with respect to a baseline. This baseline is defined by the lower envelope fitted for each individual cluster in the CN vs. M_V distribution. The left panel in Fig. 5 illustrates the baseline fit and the right panel shows the resulting δCN vs. M_V distribution for the cluster NGC 288.

In the previous sections we saw that the bimodality is only clearly detected for stars on the lower RGB. Therefore, in the following we concentrate on this part of the CMD. Figure 6 shows the histograms of the CN excess parameter for the RGB stars in all eight globular clusters in our sample, sorted by their metallicity. We selected a bin width of 0.13, comparable to the median uncertainties of the CN index for these stars.

Most of the metal-poor clusters (M 15, M 55, and M 22) show a distinct main CN-weak peak with a weak extension towards higher δCN values. For NGC 5286, we observe a fairly flat distribution. However, due to the small sample size we

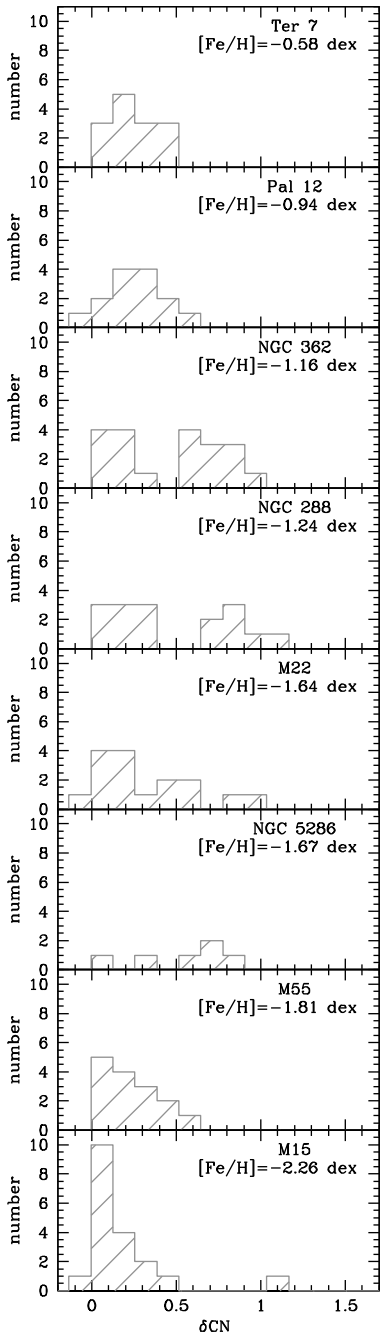

Fig. 6. Distributions of CN-band strength in the RGB stars of our sample clusters. The histograms of the CN-excess parameter δCN are plotted. The clusters are sorted by their metallicity. The two fairly metal-rich Sgr clusters are found in the two uppermost panels. The very CN-strong star in M 15 lies slightly off the RGB and therefore is probably not a cluster member.

cannot definitely comment on any distribution pattern. For NGC 288 and NGC 362, which have similar intermediate metallicities, the bimodal distribution clearly shows up in these plots. Both peaks are roughly equally pronounced. The two probable Sgr dSph clusters (Pal 12 and Ter 7) show a single peak and a fairly broad distribution around the CN-weak peak. The spanned ranges in δCN of about 0.45 and 0.53 for Ter 7 and Pal 12 are comparable with the ranges of 0.54 and 0.48 for M 55 and M 15 (excluding the extremely CN-strong outlier in the last cluster) which at first glance might point to a similar enrichment history

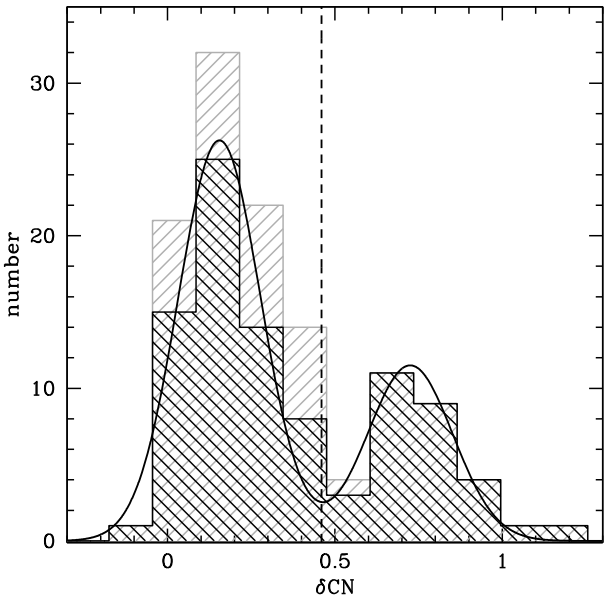

Fig. 7. Combined histograms of the CN-excess parameter for the clusters in our sample. The gray histogram comprises all eight clusters. In the black histogram Pal 12 and Ter 7, which are believed to belong to the Sgr dSph, are not included. Here we only consider stars on the lower RGB. δCN shows a bimodal distribution, which was fitted by two Gaussians. The minimum between the two Gaussians was chosen as the criterion to differentiate between CN-strong and CN-weak stars.

of those clusters, despite their very different metallicities and environments they live in. However, the apparent broadness observed in M 15 and M 55 is mainly due to the metal-poor nature of these clusters, resulting in larger errors in determining their CN strength. In contrast, for the metal-rich clusters Pal 12 and Ter 7, CN-strong stars and a bimodality are expected to clearly show up in these diagrams, if present. This makes the chemical patters of the Sgr clusters appear different from those of galactic clusters of similar metallicities (e.g., 47 Tuc) that show more pronounced CN spreads and/or bimodality.

In Fig. 7 we show combined histograms for the δCN measurements of the clusters in our sample. We distinguish between a histogram of all eight clusters and one where we did not include the two Sgr dSph clusters, Ter 7 and Pal 12. In both cases a clear bimodal distribution is visible. As Ter 7 and Pal 12 are of extragalactic origin we focused on the histogram based on six globular clusters. This distribution was used for the differentiation between CN-strong and CN-weak stars. We fitted a double Gaussian to the distribution and selected the minimum as the differential criteria between CN-strong and CN-weak stars. CN-strong stars are then those that have a CN excess greater than δCN = 0.46.

To quantify the observed bimodality in the CN line strength, we determined the parameter r introduced by Norris (1987). It gives the number ratio of CN-strong to CN-weak stars,

$$r = N_{\rm strong}/N_{\rm weak}. \quad (3)$$

Errors in r have been estimated from statistical uncertainties (adopting $\Delta N = \sqrt{N}$):

$$\Delta r = r\sqrt{1/N_{\rm weak} + 1/N_{\rm strong}}, \quad (4)$$

where $N_{\rm weak}$ and $N_{\rm strong}$ give the number of CN-weak and CN-strong stars, respectively.

Table 3. CN number ratios.

Cluster	$\frac{\rm CN_{weak}}{\rm CN_{strong}}$	$r_{\rm lowerRGB}$	$r_{\rm upperRGB}$
NGC 288	9/7	0.78 ± 0.39	
NGC 362	9/11	1.22 ± 0.55	2.46[a]
NGC 5286	2/4	2.00 ± 1.73	
NGC 6656 (M 22)	10/6	0.60 ± 0.31	0.41[b]
Ter 7	14/0	0.00 ± 0.00	
NGC 6809 (M 55)	13/2	0.15 ± 0.12	0.22[c]
NGC 7078 (M 15)	18/1	0.06 ± 0.06	
	(12/7)	(0.60 ± 0.29)	
Pal 12	13/1	0.07 ± 0.07	
NGC 104 (47 Tuc)		1.90[d]	1.8[d]
NGC 6839 (M 71)	13/9	0.69[e]	1.0[e], 0.63[g], 0.3[h]
NGC 1904 (M 79)			2.6[b]
NGC 2808			2.4[f]
NGC 3201			1.1[f]
NGC 5272 (M 3)			0.6[f]
NGC 5904 (M 5)			3.0[f]
NGC 6121 (M 4)			1.4[f]
NGC 6171 (M 107)			1.4[f]
NGC 6205 (M 13)			3.2[f]
NGC 6254 (M 10)			0.5[f]
NGC 6637			1.2[f]
NGC 6752			1.6[f]
NGC 6934			0.6[f]
NGC 7006			2-3.5[b]
NGC 7089 (M 2)			3.8[f]

[a] Smith & Mateo (1990); [b] Harbeck et al. (2003b); [c] Norris (1987); [d] Briley (1997); [e] Lee (2005); [f] Smith (2002); [g] Cohen (1999); [h] Penny et al. (1992).

For subsequent analysis, we included two additional data from literature sources. Briley (1997) determined the ratio of CN-strong to CN-weak stars for stars on the RGB in 47 Tuc. He distinguishes between RGB stars below and above the RGB bump and found very similar values of 1.9 and 1.8, respectively. For this work, we adopted the value of 1.9. Penny et al. (1992) and Lee (2005) find the r-parameter in the cluster M 71 for stars on the lower RGB to be 0.8 and 0.69, respectively. We adopted the more recent result by Lee (2005). The measurements of the number ratio of CN-strong stars on the upper RGB of M 71 range between 0.3 (Penny et al. 1992), 0.63 (Cohen 1999), and 1.0 (Lee 2005). The average value is 0.64, similar to those found on the lower RGB. Nevertheless, we have to keep in mind that the additional r-parameters are based on observations obtained with a different instrument and different index definitions.

In the upper part of Table 3, an overview of the number of stars identified as CN-strong and CN-weak is given. In the third column the r-parameters for the lower RGB of our clusters and M 71 and 47 Tuc are listed. The r-parameters range from 0.0 for Ter 7 to 2.00 for NGC 5286. The uncertainties vary from 0.07 for Pal 12 to 1.73 for NGC 5286. The large uncertainty for NGC 5286 is due to the small sample size. If one divided the stars of M 15 into CN-weak and CN-strong according to Fig. 4, its r-parameter would be 0.6 (given in brackets in Table 3). For those clusters that were part of previous studies, the r-parameters for the upper RGB are given in the last column. We find for two out of the three clusters of our sample, for which RGB studies exist, good agreement of the number ratios found on the SGB with those on the RGB. The values for NGC 362 differ by a

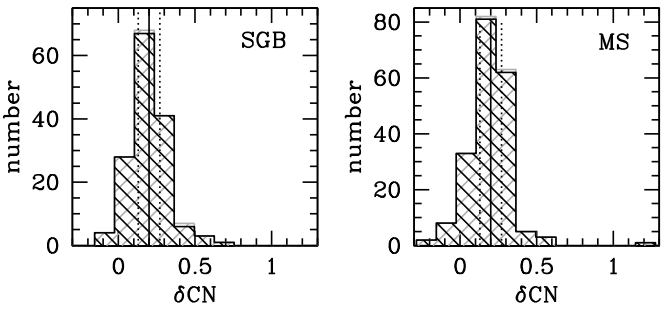

Fig. 8. The combined distributions of the CN excess parameters measured for stars on the SGB and MS. The gray histogram comprises all eight clusters. In the black histogram Pal 12 and Ter 7 are not included. The solid lines indicate the median values of the distributions. The dashed lines indicate the selection limits for CN-strong and CN-weak stars. Stars with δCN smaller than the position of the first dashed line are considered as CN-weak, stars with δCN larger than the position of the second dashed line as CN-strong.

factor of 2. The reason for this remains unclear and requires the repetition of the measurement on the RGB.

4. CN–CH–anticorrelation

In many clusters the bimodal distribution in CN is accompanied by an anticorrelation of CN and CH. A summary of this can be found in e.g., Kraft (1994). As these abundance patterns are similar to those expected by the nucleosynthesis of material in the CNO cycle, they have been attributed to a dredge-up of processed material to the stellar surfaces. In the meantime CN–CH anticorrelations have been found to be very common for clusters with a bimodal distribution in CN (see, e.g., the recent review paper by Gratton et al. 2004).

To examine possible CN–CH anticorrelations we used the distinction criteria between CN-strong and CN-weak RGB stars as described in Sect. 3.1. Although no clear bimodality in CN absorption strength was detected on the SGB and MS, we observe scatter in CN more than expected from measurement errors alone in all evolutionary states.

Since CN dichotomies have been detected before on the MS on M 13 (Briley et al. 2004), 47 Tuc (Harbeck et al. 2003a), and M 71 (Cohen 1999), it is quite conceivable that abundance variations among the less evolved stars exist in our sample as well. At the precision of our measurements, however, the signal might simply be too weak due to the higher temperatures and/or low metallicities, which inhibit the formation efficiency of the CN molecule. Nevertheless, to check for anticorrelations, we determined the CN excess parameter for the SGB and MS stars analogously to the RGB stars. The resulting δCN distributions are shown in Fig. 8. In analogy to the RGB analysis we neglected the Sgr clusters Pal 12 and Ter 7. The median δCN values were found to be 0.20 both for the SGB and MS. The standard deviation is 0.08 in both cases. We considered those stars with δCN higher than 1σ above and below the median as CN-strong and CN-weak, i.e. CN-strong: $\delta\mathrm{CN} > \mathrm{median} + \sigma$; CN-weak: $\delta\mathrm{CN} < \mathrm{median} - \sigma$.

A comparison of CN vs. M_V and CH vs. M_V is shown in Fig. 9. We differentiate between RGB, SGB, and MS stars for all clusters. Furthermore, we distinguish between stars with strong, weak, and intermediate CN absorption band features. A bimodal distribution in CH is not detected for any of the clusters. Note that even for NGC 288 and NGC 362, which showed the strongest dichotomy in CN, we do not observe a bimodality in CH. However, the CN-strong RGB stars of these two GCs clearly have smaller CH indices than the CN-weak RGB stars of similar M_V. This is not seen for the other clusters, except maybe for NGC 5286. In the case of M 22, larger uncertainties due to the significant differential reddening (Richter et al. 1999) might dilute a possible CN–CH anticorrelation. In the very metal-poor cluster, M 15, one RGB star with high CN absorption bands was identified, which also seems to be quite rich in CH. This CN- and CH-strong star in M 15 stands out from the rest of the datapoints by more than 1 in δCN. Since this star lies slightly off the RGB, we suggest that this star is not a cluster member (although it has the right radial velocity).

Moving from the RGB to the SGB and the MS, the CN–CH anticorrelation is still visible for NGC 288 and NGC 362. Due to the lower signal to noise ratio, it is less pronounced but on average the more CN-strong stars are CH-weaker. For the other clusters, no clear statement can be made.

We conclude that, in the case of clearly bimodal clusters like NGC 288 and NGC 362, the differences in the band strengths and the CN/CH anticorrelation do exist among stars of all evolutionary states. Deep mixing is believed to set in at the level of the RGB bump and does not take place in stars on the lower RGB, SGB, and MS. Furthermore, low-mass MS stars burn hydrogen only in their cores. Thus the observed patterns cannot be caused by the transport of CNO cycle processed material from the interior to the stellar surfaces. We can therefore rule out evolutionary effects within the stars as the origin of the observed anticorrelation.

5. Trends with cluster parameters

To explore possible correlations of the CN distribution with global parameters of the globular clusters, we combine our observations to quantities available in the literature. A similar analysis has been done before by, e.g., Norris (1987), Smith & Mateo (1990), Smith (2002), and Harbeck et al. (2003b). However their studies were based on compilations of upper RGB star measurements in various clusters from different sources and therefore different techniques. We now provide a sample that is based on a very homogeneous data set of eight star clusters. The cluster quantities were selected from the 2003 version of the McMaster (Harris 1996) and Pryor & Meylan (1993) globular cluster catalogs[2]. As no ellipticity is listed in these catalogs for NGC 288, we adopted the value given by Frenk & Fall (1982). The age estimates were adopted from Rosenberg et al. (1999) and Buonanno et al. (1998). Moreover, we adopted the subdivision of our globular clusters into objects belonging to different Galactic components (namely OH, YH, BD, and those accreted from the Sgr dSph (SG)) from Mackey & van den Bergh (2005). Table 4 gives an overview of the extracted parameters.

To quantify the statistical significance of possible correlations between the number ratio of CN-strong stars with various structural parameters, we computed the Spearman coefficient of rank correlation (r_s) for each parameter. This correlation coefficient is a technique that can be used to characterize the strength and direction of a relationship of two random variables. The values of r_s lie between +1 and −1, the extremes where the rank sequences completely coincide and are completely opposite, respectively. For the clusters in our sample we do not find a clear correlation between the majority of the cluster parameters and the percentage of CN-strong stars (Fig. 10).

[2] http://coihue.rutgers.edu/~andresj/gccat.html

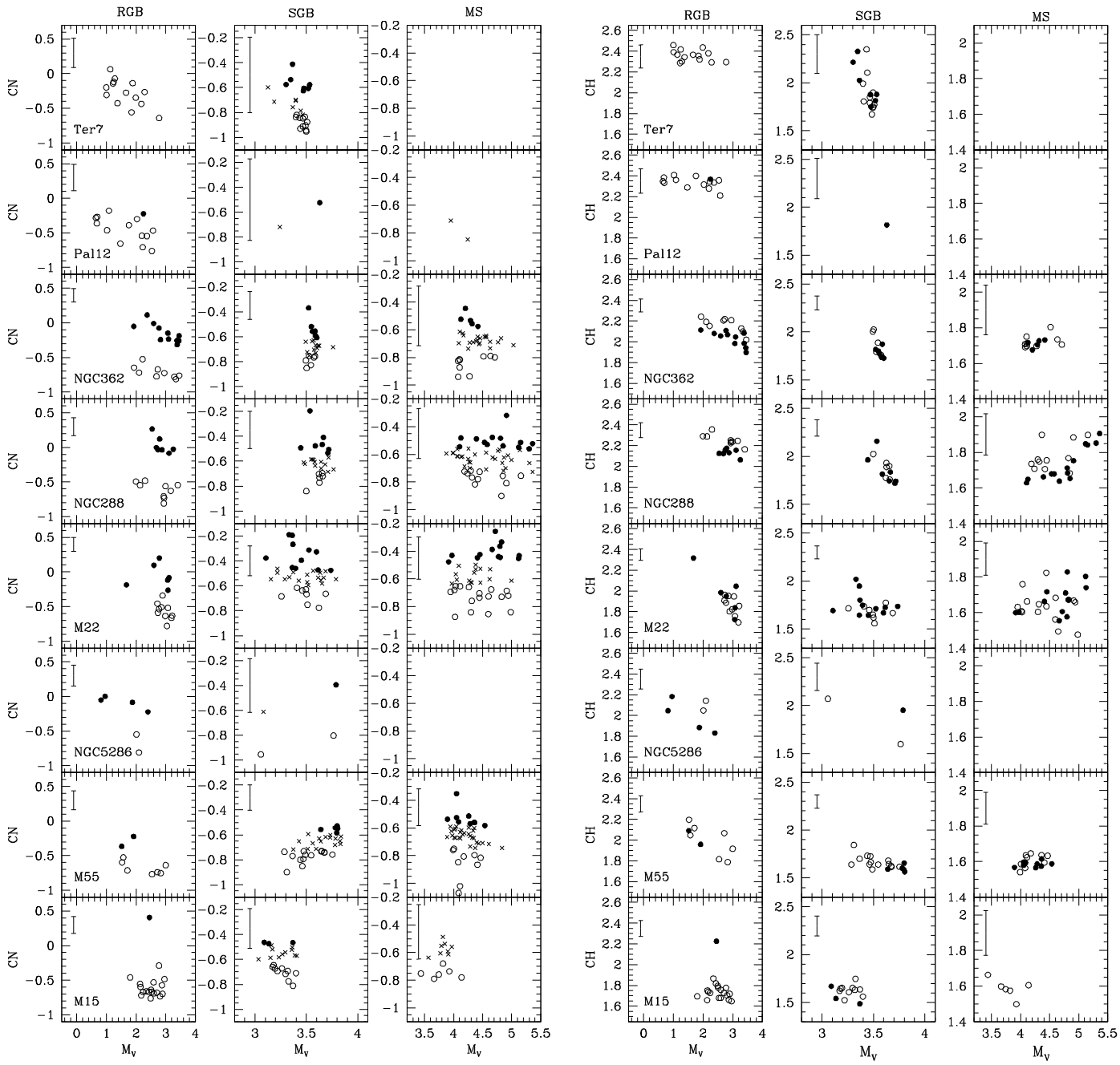

Fig. 9. The CN vs. M_V and CH vs. M_V diagrams for the eight clusters in our sample. We differentiate between RGB, SGB, and MS stars for all clusters. The CN-strong and CN-weak stars are marked by filled and open symbols, respectively. SGB and MS stars with intermediate δCN strength are plotted as crosses. For reasons of clarity these stars are only plotted in the CN vs. M_V diagrams. The median error of the measurements are given in the upper left corners of each panel. We do not plot the errors for SGB and MS stars in Pal 12 as they exceed the limit of the diagrams.

Norris (1987) observed a correlation between the percentage of CN-rich stars and the apparent flattening of the individual clusters, which he proposed is associated with the clusters' rotation. He suggested that the high systematic cluster rotation is linked via exchange of angular momentum to a higher initial angular momentum of the individual stars. Within giants the rotation may drive circulation currents that are capable of cycling the material in the envelope through the interior hydrogen-burning shell where the CNO process is active (Sweigart & Mengel 1979). Consequently a higher percentage of CN-strong stars is expected to be observed in clusters with higher mean stellar rotation velocities and thus higher overall cluster rotational velocities and hence possibly higher ellipticities. Since there is little information on cluster rotation for the globulars in our sample, we use ellipticity as a proxy for rotation. This correlation was confirmed by Smith & Mateo (1990) and Smith (2002). The computed Spearman rank coefficient of 0.26 suggests that the number ratio of CN-strong stars is mostly independent of the cluster ellipticity. We conclude that the effect proposed by Sweigart & Mengel (1979) is probably not as relevant as thought so far.

Another correlation detected by Smith & Mateo (1990) is between the r-parameter and the central velocity dispersion. Our analysis reveals $r_s = -0.07$, which makes such a correlation

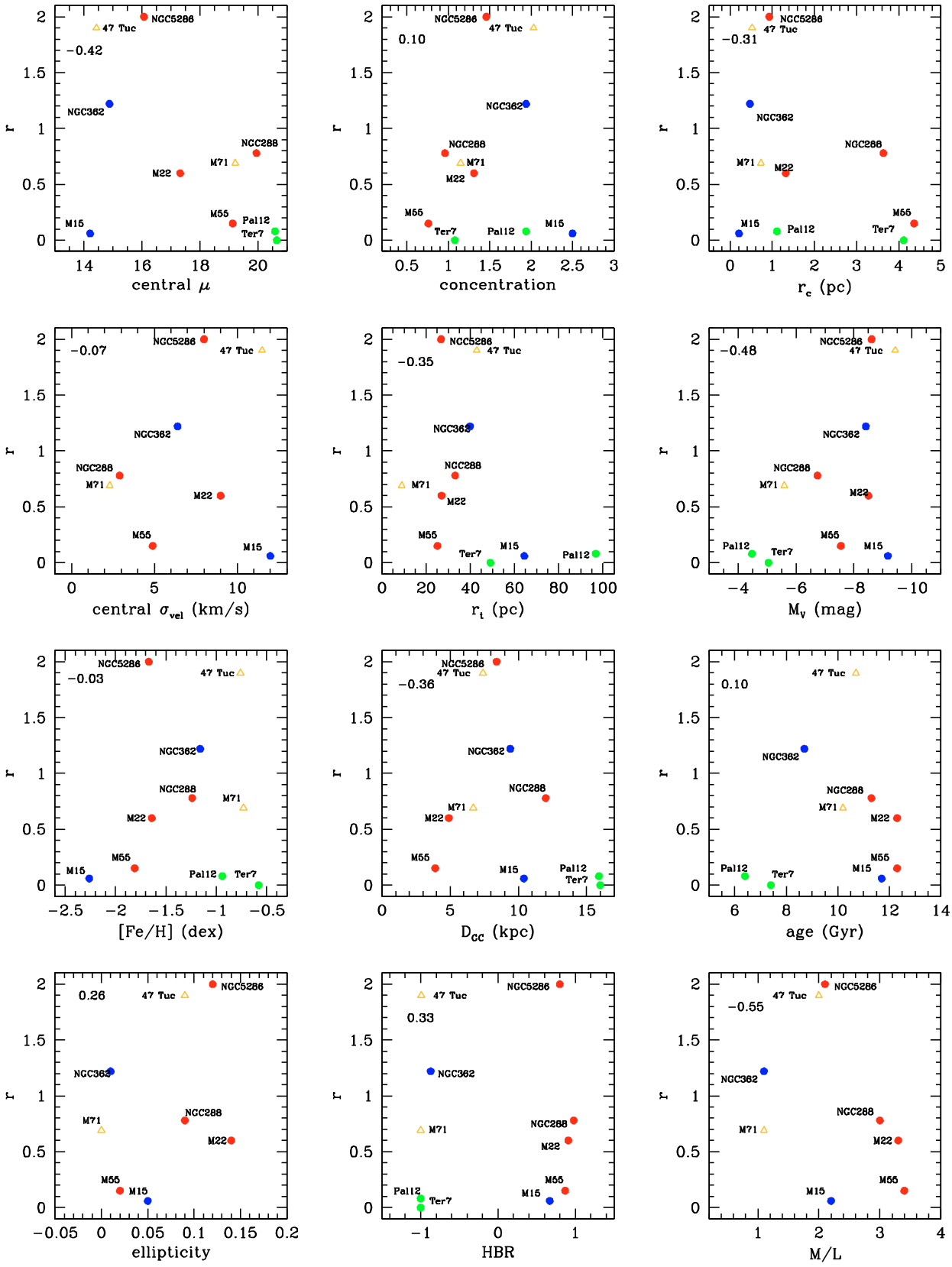

Fig. 10. The number ratio of CN-strong to CN-weak stars (r-parameter) vs. various cluster parameters (see Table 4). Our targets are indicated by the filled circles. The two results taken from the literature are marked by open triangles. Red, blue, yellow, and green colors indicate OH, YH, BD, and Sgr GCs, respectively. In the upper left corner the calculated Spearman rank correlation coefficient is given.

Table 4. Global parameters of globular clusters of our sample.

Cluster	D_{GC}^{1a} (kpc)	M_V^a (mag)	HBR^{2a}	[Fe/H]^a (dex)	c^{3a}	e^{4a}	r_{core}^{5a} (pc)	r_{tidal}^{6a} (pc)	$\mu_{0,V}^{7a}$ (mag/$''^2$)	σ^{8b} (km s^{-1})	(M/L)^b	Age^{c,d}	Class^f (Gyr)
NGC 288	12.0	–6.74	0.98	–1.24	0.96	0.09^e	3.64	33.12	19.95	2.9	3.0	11.3	OH
NGC 362	9.4	–8.41	–0.87	–1.16	1.94	0.01	0.47	39.83	14.88	6.4	1.1	8.7	YH
NGC 5286	8.4	–8.61	0.80	–1.67	1.46	0.12	0.93	26.75	16.07	8.0	2.1	NA	OH
M 22	4.9	–8.50	0.91	–1.64	1.31	0.14	1.32	26.97	17.32	9.0	3.3	12.3	OH
Terzan 7	16.0	–5.05	–1.00	–0.58	1.08	NA	4.12	49.06	20.65	NA	NA	7.4	SG
M 55	3.9	–7.55	0.87	–1.81	0.76	0.02	4.36	25.10	19.13	4.9	3.4	12.3	OH
M 15	10.4	–9.17	0.67	–2.26	2.50	0.05	0.21	64.42	14.21	12.0	2.2	12.3	YH
Palomar 12	15.9	–4.48	–1.00	–0.94	1.94	NA	1.11	96.78	20.59	NA	NA	6.4	SG
47 Tuc	7.4	–9.42	–0.99	–0.76	2.03	0.09	0.52	56.1	14.43	11.5	2.0	10.7	BD
M 71	6.7	–5.60	–1.00	–0.73	1.15	0.00	0.73	10.43	19.22	2.3	1.1	10.2	BD
NGC 1904	18.8	–7.86	0.89	–1.57	1.72	0.01	0.60	31.3	16.23	5.4	2.2	11.7	OH
NGC 2808	11.1	–9.39	–0.49	–1.15	1.77	0.12	0.73	43.42	15.17	13.4	2.4	9.3	OH
NGC 3201	8.9	–7.46	0.08	–1.58	1.30	0.12	2.08	41.38	18.77	5.2	4.1	11.3	YH
NGC 5272	12.2	–8.93	0.08	–1.57	1.84	0.04	1.66	115.5	16.34	5.6	1.2	11.3	YH
NGC 5904	6.2	–8.81	0.31	–1.27	1.83	0.14	0.92	61.96	16.05	5.7	1.4	10.9	OH
NGC 6121	5.9	–7.20	–0.06	–1.20	1.59	0.00	0.53	20.79	17.88	4.2	2.6	11.7	OH
NGC 6171	3.3	–7.13	–0.73	–1.04	1.51	0.02	1.01	32.47	18.84	4.1	3.9	11.7	OH
NGC 6205	8.7	–8.70	0.97	–1.54	1.51	0.11	1.75	56.4	16.80	7.1	2.2	11.9	OH
NGC 6254	4.6	–7.48	0.98	–1.52	1.40	0.00	1.10	27.49	17.69	6.6	3.5	11.8	OH
NGC 6637	1.9	–7.64	–1.00	–0.70	1.39	0.01	0.90	22.10	16.83	NA	NA	10.6	BD
NGC 6752	5.2	–7.73	1.00	–1.56	2.50	0.04	0.20	64.39	15.20	4.5	1.1	12.2	OH
NGC 6934	12.8	–7.46	0.25	–1.54	1.53	0.01	1.14	38.23	17.26	5.1	2.5	9.6	YH
NGC 7089	10.4	–9.02	0.96	–1.62	1.80	0.11	1.14	71.75	15.92	8.2	1.9	NA	OH
NGC 7006	38.8	–7.68	-0.28	–1.63	1.42	0.01	2.90	76.54	18.50	NA	NA	NA	YH

[1] Distance from Galactic center; [2] horizontal branch ratio: $HBR = (B-R)/(B+V+R)$; [3] concentration; [4] ellipticity $e = 1-(b/a)$; [5] core radius; [6] tidal radius; [7] central surface brightness; [8] central velocity dispersion; [a] Harris (1996); [b] Pryor & Meylan (1993); [c] Rosenberg et al. (1999); [d] Buonanno et al. (1998); [e] Frenk & Fall (1982); [f] Mackey & van den Bergh (2005).

rather unlikely. Furthermore, Smith & Mateo (1990) found the highest percentages of CN-strong stars to be restricted to the more luminous/massive clusters. They suggest an inter-cluster self-pollution scenario as a possible origin. Due to the higher binding energies in more massive clusters, the ability to retain enriched ejecta of massive and intermediate-mass stars is expected to be higher than in lower mass clusters. Our cluster sample supports the correlation with the total absolute magnitude (M_V). The calculated Spearman coefficient of $r_s = -0.48$ is actually among the highest found in our analysis.

We furthermore determined the Spearman rank correlation coefficients using the alternative higher number ratio of M 15 (see Sect. 3.2). Although most of the changes are small, some correlations show a higher significance, in particular for M_V with $r_s = -0.62$. Since the results for NGC 5286 suffer from small number statistics and thus a large error in r_s, we decided to also recalculate the correlation coefficients by neglecting this cluster (using the original value for M 15). The resulting values are comparable to those considering all clusters. An overview of the computed Spearman rank coefficients is given in Table 5.

For a more statistically complete investigation, we combined our results with those by Smith (2002) and Harbeck et al. (2003b). In Sect. 3.1 we have seen that for the majority of the studied clusters the *r*-parameter on the upper RGB is consistent with those on the lower RGB. We are thus confident that we may combine our results with those from the literature. Nevertheless we keep in mind that this leads to a more heterogeneous sample, since values of different evolutionary states and different measurements are combined.

For most parameters the lack of any clear trends is confirmed. In particular, the inclusion of our results with those listed in Smith (2002) and Harbeck et al. (2003b) further confirms the lack of a correlation between cluster ellipticity ϵ and the number ratio of CN-strong stars. We observe a large scatter in Fig. 11 (lower right panel). It can, however, not be ruled out that some clusters with low ϵ and high *r* values are actually more elliptical but appear round due to projection effects. This would dilute a possible correlation. GCs with high ϵ and low *r* values would then be clear outliers.

We see a possible connection between the *r*-parameter and the tidal radius (Fig. 11, lower left panel). Clusters with larger tidal radii seem to possess a higher percentage of CN-strong stars. Interestingly, those clusters that do not follow this trend are those that are thought to be linked to the Sgr dSph (Palomar 12 and Terzan 7), as well as the very metal-poor clusters M 15 and NGC 5272, which belong to the young halo GCs. We computed the Spearman coefficient including and excluding these cluster. The resulting values are 0.19 and 0.67, respectively. This is an interesting finding, since Zinn (1993) postulated that the young halo population of globular clusters was predominantly formed by accretion of extragalactic objects. We therefore put forward the hypothesis that, among other parameters, environmental differences due to different cluster formation sites may influence the today observed abundance patterns. Carretta (2006) showed that, apart from differences in the environmental properties during the time of formation also differences in the evolution of clusters have probably influenced the light element abundance ratios. Using a set of high-resolution spectroscopic abundance measurements he found that clusters with larger orbital semi major axes, i.e., extended orbits and revolution periods, exhibit a larger amount of inhomogeneities. From this he concluded that, for clusters on orbits reaching large Galactocentric distances,

Table 5. Calculated Spearman rank correlation coefficients.

	All clusters	Alternative value for M 15	Without NGC 5286
$\mu_{0,V}$	−0.42	−0.58	−0.38
c	0.10	0.24	0.07
$r_{\rm core}$	−0.31	−0.48	−0.30
σ	−0.03	0.05	−0.14
$r_{\rm tidal}$	−0.35	−0.27	−0.27
M_V	−0.48	−0.62	−0.43
[Fe/H]	−0.03	−0.12	0.10
$D_{\rm GC}$	−0.36	−0.31	−0.38
age	0.10	0.18	0.10
e	0.26	0.29	0.07
HBR	0.33	0.36	0.32
M/L	−0.55	−0.62	−0.57

the lack of disturbance by the Galactic disk helps to retain pre-enriched material. In contrast, clusters close to the Galactic center might have suffered early and frequent disk/bulge shocks that enforced rapid gas loss and prohibited the formation of a second enriched subpopulation. Those clusters also show smaller tidal radii due to the even stronger tidal forces towards the center of the Galaxy.

In the upper right panel of Fig. 11, we plotted the r-parameter as a function of the absolute magnitude, representing the present-day cluster mass. It seems that the maximum number ratio of CN-strong to CN-weak stars increases with increasing M_V (cf. Smith 2002). Only the brightest clusters have formed CN-strong stars. This supports the idea that the more massive objects can more efficiently retain processed material ejected from evolved stars.

The possible CN-bimodality of M 15 as described in Sect. 3.2 and shown in Fig. 4 increases the r-parameter of this cluster to 0.6. As a consequence the correlations of r with absolute magnitude, M_V and tidal radius, $r_{\rm t}$ become slightly more significant with Spearman rank values of $r_{\rm s} = -0.56$ and -0.68, respectively. The low correlations with central velocity dispersion and ellipticity, however, remain nearly unchanged. More accurate CN/CH index measurements of this very metal-poor cluster are needed to confirm these findings.

6. Summary and conclusions

We analyzed the absorption bands of the CN and CH molecule in eight Galactic globular clusters via line index measurements. In each cluster, stars of various evolutionary stages were studied, from the lower RGB and SGB to the upper MS. Our sample comprises clusters belonging to different Milky Way components, e.g., young and old halos. In particular, two of our studied objects are associated with a disrupting Galactic companion, the Sagittarius dwarf spheroidal (Sgr dSph). We could show that the majority of the studied clusters shows significant CN/CH variations at the base of the RGB. For the two most prominent CN-bimodal GCs, NGC 288 and NGC 362, CN anticorrelates with CH. A weak signal for a CN/CH anticorrelation was detected also in the least evolved stars in these clusters. From this we conclude that purely evolutionary effects within the stellar interior cannot be the main driver of the observed abundance patterns. Our findings therefore favor a scenario in which a certain fraction of most clusters was formed out of material that was enriched or polluted by ejecta of a prior generation of massive stars. In fact, the existence of star-to-star variations among those slightly evolved stars favors self-enrichment as the probable origin. One possible explanation could be that the stars observed nowadays in globular clusters formed from protocluster material that was to some degree inhomogeneously enriched in light elements. Such a pollution might have originated from ejecta of a prior generation of massive and therefore fast evolving stars, either belonging to the cluster itself or to the field population of a larger (dwarf sized) galaxy in which the cluster was embedded (e.g., Bekki et al. 2007). Possible candidates for the polluters discussed in the literature are massive AGB stars (e.g., Cottrell & Da Costa 1981; Ventura et al. 2001) and more recently fast rotating massive stars (Decressin et al. 2007). AGBs eject material via slow winds that are processed through the hot CNO cycle but are not enriched in iron. Fast rotating massive stars lose large amounts of material through slow winds, which are also enriched in H-burning products.

For the clusters NGC 288 and NGC 362, we found a clear bimodal distribution in CN with similar numbers of CN-strong and CN-weak stars. As the two clusters are a second-parameter pair, we conclude that the horizontal branch morphology is not correlated with this phenomenon. A possible explanation for such a pronounced dichotomy is given by a prolonged star formation in these globular clusters. The second, enriched stellar population formed well after the first generation had expelled and homogeneously distributed their AGB ejecta. The existence of such multiple stellar populations within globular clusters is further supported by the recent discoveries of complex CMD morphologies (e.g., multiple SGBs and MSs with age spreads) in some massive objects (Bedin et al. 2004; Piotto et al. 2007).

The two probable former Sgr dSph clusters (Terzan 7 and Palomar 12) do not exhibit any CN-strong stars. They are the most metal-rich clusters in our sample, so the double metal molecule CN should be easy to detect. We conclude that these clusters might lack stars with strong CN absorption. Our results suggest that the accreted Sgr globular clusters might be more chemically homogeneous than those native to the Milky Way. This is supported by the abundance analysis of 21 elements for four Sgr stars by Cohen (2004), who do not find a significant star-to-star scatter. Probably environmental conditions during the formation of the clusters played a major role for the observed abundance pattern. However, we point out that all existing studies suffer from small number statistics. Thus it cannot be ruled out that CN-rich stars are simply missed in the sampling (see the preliminary results by Briley et al. 2007). For more conclusions a thorough investigation of the abundance patterns other probable Sgr clusters (M 54, Arp 2, Ter 7, Ter 8, and Pal 12) is desirable.

To search for possible drivers for the abundance anomalies we studied the ratio of CN-strong/CN-weak stars as a function of various cluster parameters. We do not confirm the correlation with the cluster ellipticity that was observed before (Norris 1987). Our study therefore does not support cluster rotation and the associated enhanced deep mixing (Sweigart & Mengel 1979) as a main source of the production of CN-strong stars. Although we hardly see correlations in the number ratio of CN-strong stars with the majority of cluster parameters, some dependencies do seem to exist. We find evidence of an increase in the CN-strong star fraction with cluster tidal radius. Since GCs with large tidal radii are mostly found in the weak tidal field of the Galaxy (well outside the bulge and disk potential), they might occupy orbits that avoid bulge/disk shocks. Thus they might keep their gas longer, which favors the build-up of a second generation of enriched stars. Furthermore, we find that preferably the more luminous/massive clusters exhibit a large number of CN-strong stars. This may be an indication that the CNO processed ejecta could be more efficiently retained by more massive objects,

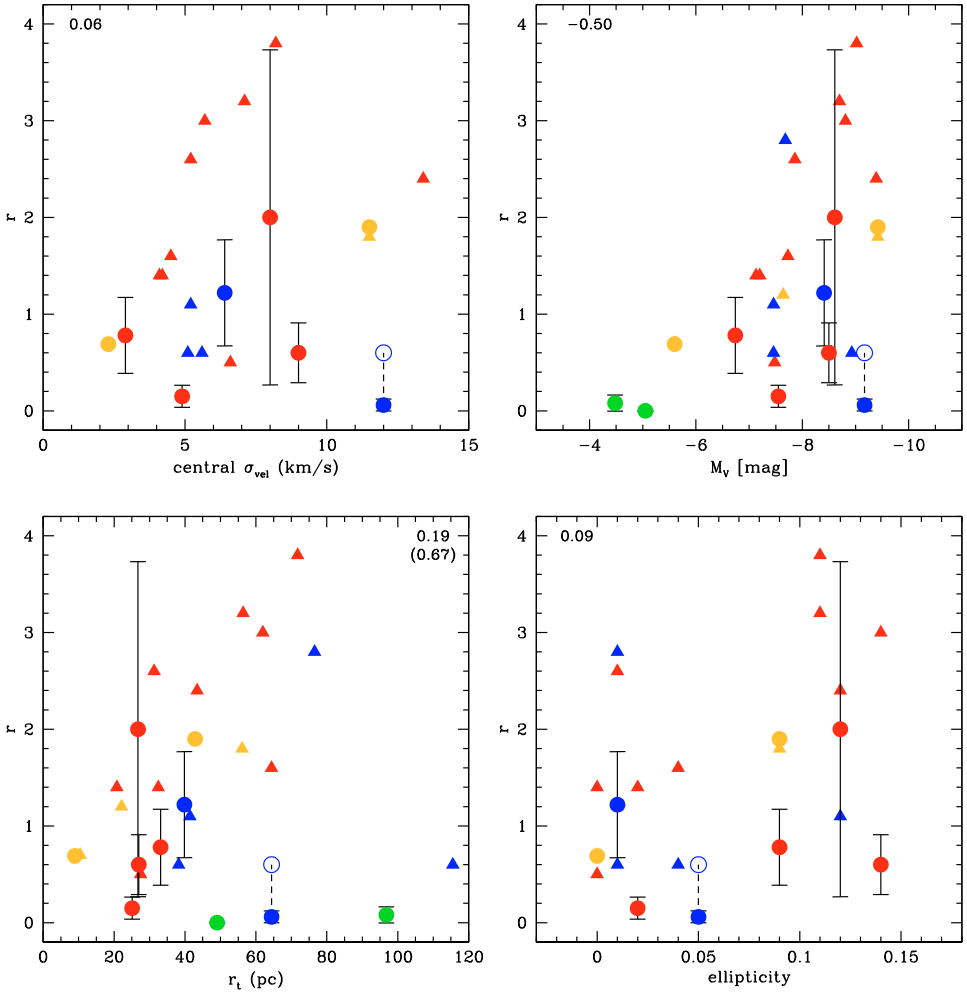

Fig. 11. Plot of the r-parameter vs. those globular cluster parameters that showed a promising correlation in Fig. 10 or in previous studies by e.g., Smith (2002), such as ellipticity, central velocity dispersion (σ_{vel}), absolute brightness (M_V), and tidal radius r_t. We also include the results by Smith (2002) (triangles). The results of our study are plotted as filled circles. In this figure we furthermore differentiate between the different MW cluster populations. Old and young halo clusters are colored in red and blue, respectively. Bulge and disk clusters are plotted in yellow and accreted clusters from dwarf galaxies, such as the Sagittarius dSph, in green. The open blue circle indicates the alternative value of the r-parameter for M 15.

independent of their tidal radius. The picture emerges that there are two basic channels that lead to a high fraction of CN-rich stars in GCs: 1) the cluster formed and lived in a remote environment, which allowed it to keep/regain its gas; and 2) the gravitational potential of the cluster itself was large enough to trap the enriched ejecta of slow velocity winds out of which a new generation of stars was formed.

Interestingly, those clusters that do not follow the observed trend are either associated with the young halo or accreted from the Sgr dSph. This might indicate that, as third parameter, the environmental conditions in which the clusters formed might had a non-negligible influence on the abundance patterns we observe today.

Nevertheless we point out that our study is limited to a small sample of clusters. For a statistically better supported study, a larger cluster sample is necessary. Furthermore, a complete set of cluster parameters is needed to search for the significance of the CN-CH differences between genuine halo globular clusters and accreted objects.

Acknowledgements. The authors thank the referee for the useful comments and suggestions. A.K. and E.K.G. gratefully acknowledge support by the Swiss National Science Foundation through the grants 200020-105260 and 200020-113697. M.H. acknowledges support from a German Science Foundation Grant (DFG-Projekt HI-855/2).

Appendix A: List of spectroscopic sample stars

The following table contains a magnitude limited list (five stars per cluster) of our spectroscopic sample stars. They are ordered by increasing V magnitude. The columns are as follows:

Column 1. Identification of the object, giving the name of the globular cluster followed by a number which is ordered with increasing V magnitude.

Column 2. Right ascension for the epoch 2000 in decimals.

Column 3. Declination (2000) in decimals.

Column 4. Apparent V magnitude as determined by PSF photometry with DAOPHOT II under IRAF.

Column 5. $B - V$ color from PSF photometry.

Column 6. Measured CN band strength.

Column 7. Error in measured CN band strength.

Column 8. Measured CH band strength.

Column 9. Error in measured CH band strength.

Column 10. Calculated CN-excess parameter δCN.

Column 11. Radial velocity as determined from cross-correlation with FXCOR under IRAF and not corrected for systematic errors. Thus, these velocities are only indicative.

Table A.1. List of spectroscopic sample stars, ordered by increasing V magnitude.

Id	α(2000)	δ(2000)	V	$B-V$	CN	dCN	CH	dCH	δCN	$v_{\rm rad}$	Type
NGC 288-001	13.23449	−26.53142	16.83	0.76	−0.493	0.105	2.291	0.056	0.303	−90.9	RGB
NGC 288-002	13.22360	−26.59697	16.97	0.78	−0.546	0.094	2.288	0.052	0.252	−91.1	RGB
NGC 288-003	13.20552	−26.63372	17.14	0.76	−0.482	0.082	2.355	0.049	0.319	−83.4	RGB
NGC 288-004	13.22098	−26.54228	17.37	0.71	0.265	0.130	2.125	0.063	1.070	−89.1	RGB
NGC 288-005	13.22482	−26.60748	17.52	0.73	−0.004	0.120	2.124	0.063	0.803	−94.3	RGB
...	...	...	...	...	...	...	...	...	...	...	...
NGC 362-001	15.70094	−70.86414	16.73	0.81	−0.051	0.066	2.115	0.039	0.822	219.7	RGB
NGC 362-002	15.62026	−70.90492	16.74	0.80	−0.648	0.064	2.243	0.040	0.225	202.7	RGB
NGC 362-003	15.70814	−70.83189	16.92	0.79	−0.720	0.071	2.193	0.044	0.154	221.1	RGB
NGC 362-004	15.69642	−70.87922	17.03	0.78	−0.525	0.072	2.153	0.046	0.350	206.1	RGB
NGC 362-005	15.73940	−70.84594	17.18	0.80	0.115	0.087	2.081	0.049	0.990	199.7	RGB
...	...	...	...	...	...	...	...	...	...	...	...
NGC 5286-001	206.54955	−51.42272	16.77	1.08	−0.051	0.099	2.047	0.057	0.741	90.0	RGB
NGC 5286-002	206.54435	−51.40362	16.91	1.07	0.002	0.104	2.183	0.059	0.796	84.1	RGB
NGC 5286-003	206.53143	−51.40539	17.83	0.97	−0.085	0.144	1.884	0.083	0.724	88.7	RGB
NGC 5286-004	206.56119	−51.42629	17.96	1.03	−0.549	0.150	2.049	0.096	0.262	86.2	RGB
NGC 5286-005	206.56752	−51.42112	18.05	0.96	−0.810	0.152	2.141	0.096	0.002	73.4	RGB
...	...	...	...	...	...	...	...	...	...	...	...
M 22-001	279.02891	−23.91745	15.28	0.79	−0.187	0.066	2.316	0.035	0.483	−125.7	RGB
M 22-002	279.04091	−23.91550	16.20	0.80	0.096	0.100	1.984	0.052	0.802	−147.9	RGB
M 22-003	279.05050	−23.92792	16.32	0.77	−0.459	0.100	1.908	0.054	0.252	−141.3	RGB
M 22-004	279.05276	−23.92067	16.33	0.79	−0.589	0.099	1.961	0.056	0.122	−132.7	RGB
M 22-005	279.05760	−23.88352	16.38	0.84	0.199	0.098	1.949	0.051	0.913	−136.2	RGB
...	...	...	...	...	...	...	...	...	...	...	...
Ter7-001	289.40929	−34.65456	16.82	1.22	0.350	0.129	2.425	0.054	0.396	125.9	RGB
Ter7-002	289.43408	−34.67519	16.95	1.19	0.050	0.128	2.366	0.057	0.128	139.2	RGB
Ter7-003	289.44845	−34.65597	17.42	1.08	0.179	0.152	2.412	0.069	0.371	138.5	RGB
Ter7-004	289.44580	−34.64778	17.51	1.10	0.147	0.145	2.399	0.070	0.361	147.0	RGB
Ter7-005	289.41804	−34.68052	17.53	0.98	−0.265	0.119	2.304	0.065	−0.046	138.1	RGB
...	...	...	...	...	...	...	...	...	...	...	...
M 15-001	322.52784	12.19498	17.17	0.72	−0.459	0.093	1.695	0.057	0.278	−128.5	RGB
M 15-002	322.56545	12.21040	17.51	0.71	−0.553	0.105	1.659	0.066	0.188	−128.7	RGB
M 15-003	322.53617	12.13113	17.52	0.67	−0.598	0.097	1.751	0.064	0.143	−98.6	RGB
M 15-004	322.53279	12.18582	17.55	0.71	−0.718	0.111	1.740	0.070	0.023	−111.0	RGB
M 15-005	322.54196	12.15207	17.61	0.67	−0.670	0.113	1.729	0.072	0.072	−107.7	RGB
...	...	...	...	...	...	...	...	...	...	...	...
Pal12-001	326.66154	−21.24816	16.21	0.90	−0.197	0.100	2.273	0.052	0.227	−5.7	RGB
Pal12-002	326.66939	−21.23127	16.61	0.88	0.151	0.105	2.509	0.057	0.627	8.5	RGB
Pal12-003	326.65155	−21.24316	16.88	0.79	−0.578	0.108	2.208	0.062	−0.068	14.0	RGB
Pal12-004	326.67071	−21.25261	16.92	0.75	−0.442	0.094	2.121	0.056	0.073	18.5	RGB
Pal12-005	326.67863	−21.26354	16.97	0.74	−0.567	0.095	2.068	0.058	−0.045	17.5	RGB
...	...	...	...	...	...	...	...	...	...	...	...

Column 12. "Type" describes to which part of the CMD the star most probably belongs: RGB = red giant branch, HB = horizontal branch, SGB = sub giant branch, MS = main sequence.

Note: The full table of analyzed stars only is available in the online version of the article.

References

Alcaino, G., Liller, W., & Alvarado, F. 1997, AJ, 114, 2626
Alcaino, G., Liller, W., Alvarado, F., & Wenderoth, E. 1992, AJ, 104, 190
Bedin, L. R., Piotto, G., Anderson, J., et al. 2004, ApJ, 605, L125
Bekki, K., Campbell, S. W., Lattanzio, J. C., & Norris, J. E. 2007, MNRAS, 377, 335
Bellazzini, M., Pecci, F. F., Ferraro, F. R., et al. 2001, AJ, 122, 2569
Bellazzini, M., Ferraro, F. R., & Ibata, R. 2003, AJ, 125, 188
Briley, M. M. 1997, AJ, 114, 1051
Briley, M. M., Bell, R. A., Smith, G. H., & Hesser, J. E. 1989, ApJ, 341, 800
Briley, M. M., Harbeck, D., Smith, G. H., & Grebel, E. K. 2004, AJ, 127, 1588
Briley, M. M., Martell, S., & Smith, G. H. 2007, in Amer. Astron. Soc. Meet. Abst., 211, 31
Buonanno, R., Corsi, C. E., Pulone, L., et al. 1995, AJ, 109, 663
Buonanno, R., Corsi, C. E., Pulone, L., Fusi Pecci, F., & Bellazzini, M. 1998, A&A, 333, 505
Carretta, E. 2006, AJ, 131, 1766
Charbonnel, C. 1995, ApJ, 453, L41
Cohen, J. G. 1978, ApJ, 223, 487
Cohen, J. G. 1999, AJ, 117, 2434
Cohen, J. G. 2004, AJ, 127, 1545
Cottrell, P. L., & Da Costa, G. S. 1981, ApJ, 245, L79
D'Antona, F., Gratton, R., & Chieffi, A. 1983, Mem. SAIt, 54, 173
D'Antona, F., Caloi, V., Montalbán, J., Ventura, P., & Gratton, R. 2002, A&A, 395, 69
D'Antona, F., Bellazzini, M., Caloi, V., et al. 2005, ApJ, 631, 868
Decressin, T., Meynet, G., Charbonnel, C., Prantzos, N., & Ekström, S. 2007, A&A, 464, 1029
Denissenkov, P. A., & Herwig, F. 2003, ApJ, 590, L99
Denissenkov, P. A., & VandenBerg, D. A. 2003, ApJ, 593, 509
Durrell, P. R., & Harris, W. E. 1993, AJ, 105, 1420
Frenk, C. S., & Fall, S. M. 1982, MNRAS, 199, 565
Fulbright, J. P. 2002, AJ, 123, 404
Gratton, R. G., Sneden, C., Carretta, E., & Bragaglia, A. 2000, A&A, 354, 169
Gratton, R., Sneden, C., & Carretta, E. 2004, ARA&A, 42, 385
Harbeck, D., Smith, G. H., & Grebel, E. K. 2003a, AJ, 125, 197
Harbeck, D., Smith, G. H., & Grebel, E. K. 2003b, A&A, 409, 553
Harris, W. E. 1996, AJ, 112, 1487
Hilker, M., Kayser, A., Richtler, T., & Willemsen, P. 2004, A&A, 422, L9

Iben, Jr., I. 1968, Nature, 220, 143
Kayser, A., Hilker, M., Richtler, T., & Willemsen, P. G. 2006, A&A, 458, 777
Kraft, R. P. 1994, PASP, 106, 553
Lee, S. G. 2000, J. Korean Astron. Soc., 33, 137
Lee, S. G. 2005, J. Korean Astron. Soc., 38, 23
Mackey, A. D., & van den Bergh, S. 2005, MNRAS, 360, 631
Maeder, A., & Meynet, G. 2006, A&A, 448, L37
Norris, J. 1987, ApJ, 313, L65
Norris, J., & Smith, G. H. 1981, in Astrophysical Parameters for Globular Clusters, ed. A. G. D. Philip, & D. S. Hayes, IAU Coll., 68, 109
Osborn, W. 1971, The Observatory, 91, 223
Penny, A. J., Smith, G. H., & Churchill, C. W. 1992, MNRAS, 257, 89
Piotto, G., Bedin, L. R., Anderson, J., et al. 2007, ApJ, 661, L53
Pritzl, B. J., Venn, K. A., & Irwin, M. 2005, AJ, 130, 2140
Pryor, C., & Meylan, G. 1993, in Structure and Dynamics of Globular Clusters, ASP Conf. Ser., 50, 357
Richter, P., Hilker, M., & Richtler, T. 1999, A&A, 350, 476
Rosenberg, A., Saviane, I., Piotto, G., & Aparicio, A. 1999, AJ, 118, 2306
Samus, N., Ipatov, A., Smirnov, O., et al. 1995a, A&AS, 112, 439
Samus, N., Kravtsov, V., Pavlov, M., Alcaino, G., & Liller, W. 1995b, A&AS, 109, 487
Sbordone, L., Bonifacio, P., Marconi, G., Buonanno, R., & Zaggia, S. 2005, A&A, 437, 905
Sbordone, L., Bonifacio, P., Buonanno, R., et al. 2007, A&A, 465, 815
Shetrone, M. D., Côté, P., & Sargent, W. L. W. 2001, ApJ, 548, 592
Smith, G. H. 2002, PASP, 114, 1215
Smith, G. H., & Martell, S. L. 2003, PASP, 115, 1211
Smith, G. H., & Mateo, M. 1990, ApJ, 353, 533
Smith, G. H., & Norris, J. 1982, ApJ, 254, 149
Smith, G. H., & Norris, J. 1983, ApJ, 264, 215
Smith, G. H., Shetrone, M. D., Bell, R. A., Churchill, C. W., & Briley, M. M. 1996, AJ, 112, 1511
Stetson, P. B., Hesser, J. E., Smith, G. H., Vandenberg, D. A., & Bolte, M. 1989, AJ, 97, 1360
Suntzeff, N. B. 1981, ApJS, 47, 1
Sweigart, A. V., & Mengel, J. G. 1979, ApJ, 229, 624
Thoul, A., Jorissen, A., Goriely, S., et al. 2002, A&A, 383, 491
Ventura, P., D'Antona, F., Mazzitelli, I., & Gratton, R. 2001, ApJ, 550, L65
Weiss, A., Denissenkov, P. A., & Charbonnel, C. 2000, A&A, 356
Willemsen, P. G., Hilker, M., Kayser, A., & Bailer-Jones, C. A. L. 2005, A&A, 436, 379
Zinn, R. 1985, ApJ, 293, 424
Zinn, R. 1993, in The Globular Cluster-Galaxy Connection, ed. G. H. Smith, & J. P. Brodie, ASP Conf. Ser., 48, 38

Table A.1. List of spectroscopic sample stars, ordered by increasing V magnitude.

Id	α(2000)	δ(2000)	V	$B-V$	CN	dCN	CH	dCH	δCN	$v_{\rm rad}$	Type
NGC 288-001	13.23449	−26.53142	16.83	0.76	−0.493	0.105	2.291	0.056	0.303	−90.9	RGB
NGC 288-002	13.22360	−26.59697	16.97	0.78	−0.546	0.094	2.288	0.052	0.252	−91.1	RGB
NGC 288-003	13.20552	−26.63372	17.14	0.76	−0.482	0.082	2.355	0.049	0.319	−83.4	RGB
NGC 288-004	13.22098	−26.54228	17.37	0.71	0.265	0.130	2.125	0.063	1.070	−89.1	RGB
NGC 288-005	13.22482	−26.60748	17.52	0.73	−0.004	0.120	2.124	0.063	0.803	−94.3	RGB
NGC 288-006	13.23787	−26.52769	17.57	0.70	−0.034	0.128	2.158	0.066	0.774	−94.7	RGB
NGC 288-007	13.23132	−26.57133	17.62	0.72	0.121	0.110	2.176	0.060	0.930	−79.7	RGB
NGC 288-008	13.24678	−26.52963	17.71	0.69	−0.034	0.137	2.133	0.071	0.776	−91.9	RGB
NGC 288-009	13.22385	−26.56176	17.76	0.72	−0.707	0.159	2.251	0.085	0.105	−90.1	RGB
NGC 288-010	13.23367	−26.62778	17.77	0.72	−0.812	0.115	2.225	0.067	0.000	−104.1	RGB
NGC 288-011	13.23598	−26.59420	17.78	0.69	−0.731	0.125	2.237	0.071	0.081	−92.5	RGB
NGC 288-012	13.23494	−26.57646	17.82	0.72	−0.560	0.136	2.238	0.075	0.253	−88.3	RGB
NGC 288-013	13.23544	−26.54812	17.94	0.69	−0.083	0.142	2.157	0.076	0.732	−84.5	RGB
NGC 288-014	13.22266	−26.61854	18.00	0.71	−0.628	0.155	2.245	0.086	0.188	−100.1	RGB
NGC 288-015	13.23266	−26.58919	18.09	0.68	−0.028	0.144	2.064	0.078	0.789	−84.7	RGB
NGC 288-016	13.21534	−26.56422	18.24	0.66	−0.547	0.158	2.165	0.087	0.273	−88.0	RGB
NGC 288-017	13.25406	−26.61293	18.27	0.59	−0.492	0.162	1.964	0.087	0.328	−95.9	SGB
NGC 288-018	13.23324	−26.53597	18.31	0.62	−0.610	0.169	2.078	0.095	0.211	−92.4	SGB
NGC 288-019	13.24789	−26.60889	18.32	0.59	−0.623	0.146	1.970	0.084	0.198	−88.6	SGB
NGC 288-020	13.23613	−26.59022	18.33	0.61	−0.840	0.139	2.025	0.081	−0.019	−92.1	SGB
NGC 288-021	13.22914	−26.53786	18.36	0.59	−0.197	0.174	2.158	0.094	0.625	−86.8	SGB
NGC 288-022	13.23485	−26.58387	18.38	0.58	−0.585	0.149	1.842	0.083	0.237	−85.4	SGB
NGC 288-023	13.23269	−26.62510	18.39	0.52	−0.584	0.143	1.824	0.081	0.238	−89.8	SGB
NGC 288-024	13.23434	−26.58061	18.40	0.57	−0.588	0.152	1.994	0.088	0.234	−87.6	SGB
NGC 288-025	13.20622	−26.63090	18.41	0.54	−0.605	0.115	1.853	0.072	0.217	−82.6	SGB
NGC 288-026	13.23036	−26.54462	18.42	0.52	−0.636	0.155	1.942	0.087	0.187	−84.9	SGB
NGC 288-027	13.23675	−26.53481	18.42	0.47	−0.476	0.136	1.815	0.080	0.346	−74.4	SGB
NGC 288-028	13.24216	−26.62313	18.45	0.48	−0.704	0.151	1.776	0.086	0.119	−95.7	SGB
NGC 288-029	13.22620	−26.53989	18.46	0.52	−0.773	0.153	1.932	0.087	0.050	−81.6	SGB
NGC 288-030	13.24081	−26.57897	18.46	0.53	−0.731	0.164	1.889	0.093	0.092	−85.4	SGB
NGC 288-031	13.22603	−26.58213	18.47	0.53	−0.658	0.167	1.879	0.092	0.165	−84.0	SGB
NGC 288-032	13.23301	−26.61150	18.47	0.49	−0.604	0.156	1.764	0.088	0.219	−90.6	SGB
NGC 288-033	13.20604	−26.54595	18.48	0.49	−0.695	0.143	1.899	0.084	0.128	−82.1	SGB
NGC 288-034	13.22852	−26.61737	18.48	0.49	−0.466	0.152	1.744	0.087	0.358	−96.6	SGB
NGC 288-035	13.23424	−26.63550	18.49	0.50	−0.720	0.139	1.758	0.083	0.104	−99.5	SGB
NGC 288-036	13.23346	−26.56777	18.50	0.50	−0.409	0.148	1.837	0.086	0.415	−82.0	SGB
NGC 288-037	13.24172	−26.56576	18.51	0.51	−0.626	0.162	1.883	0.090	0.198	−80.9	SGB
NGC 288-038	13.20516	−26.55748	18.54	0.49	−0.684	0.147	1.859	0.085	0.141	−80.0	SGB
NGC 288-039	13.23552	−26.61578	18.54	0.47	−0.535	0.140	1.720	0.081	0.290	−86.8	SGB
NGC 288-040	13.23028	−26.52377	18.55	0.48	−0.571	0.146	1.786	0.086	0.253	−85.0	SGB
NGC 288-041	13.21876	−26.55923	18.55	0.49	−0.506	0.144	1.741	0.082	0.319	−75.0	SGB
NGC 288-042	13.20784	−26.55264	18.60	0.47	−0.666	0.135	1.742	0.080	0.159	−73.1	SGB
NGC 288-043	13.23634	−26.53191	18.71	0.46	−0.595	0.134	1.749	0.083	0.232	−68.2	MS
NGC 288-044	13.24177	−26.58093	18.82	0.43	−0.591	0.140	1.774	0.089	0.238	−66.3	MS
NGC 288-045	13.23973	−26.53821	18.83	0.44	−0.592	0.141	1.722	0.088	0.238	−66.3	MS
NGC 288-046	13.23891	−26.52848	18.89	0.44	−0.613	0.147	1.697	0.092	0.217	−70.5	MS
NGC 288-047	13.24374	−26.59485	18.89	0.47	−0.562	0.139	1.705	0.090	0.268	−66.3	MS
NGC 288-048	13.22868	−26.55067	18.90	0.43	−0.617	0.143	1.708	0.089	0.214	−71.3	MS
NGC 288-049	13.22868	−26.55067	18.90	0.43	−0.617	0.143	1.708	0.089	0.214	−71.3	MS
NGC 288-050	13.24387	−26.60358	18.93	0.45	−0.545	0.142	1.629	0.090	0.286	−65.5	MS
NGC 288-051	13.24115	−26.59677	18.96	0.43	−0.481	0.138	1.648	0.090	0.350	−69.8	MS
NGC 288-052	13.25602	−26.60595	18.96	0.46	−0.619	0.147	1.739	0.096	0.213	−73.6	MS
NGC 288-053	13.24202	−26.58934	18.98	0.45	−0.614	0.140	1.671	0.093	0.218	−57.9	MS
NGC 288-054	13.22418	−26.53314	19.02	0.45	−0.725	0.151	1.735	0.095	0.108	−62.4	MS
NGC 288-055	13.23348	−26.60758	19.02	0.46	−0.689	0.150	1.704	0.097	0.144	−77.0	MS
NGC 288-056	13.23161	−26.60188	19.07	0.45	−0.739	0.160	1.707	0.102	0.095	−59.7	MS
NGC 288-057	13.25071	−26.61296	19.08	0.43	−0.632	0.162	1.759	0.102	0.202	−76.9	MS
NGC 288-058	13.23847	−26.63385	19.09	0.43	−0.559	0.141	1.648	0.095	0.274	−67.6	MS
NGC 288-059	13.24501	−26.57766	19.10	0.45	−0.656	0.172	1.780	0.106	0.178	−78.9	MS
NGC 288-060	13.24804	−26.62716	19.11	0.43	−0.658	0.148	1.685	0.096	0.176	−64.7	MS
NGC 288-061	13.23127	−26.60001	19.11	0.46	−0.700	0.161	1.716	0.104	0.134	−69.0	MS
NGC 288-062	13.22175	−26.54475	19.13	0.45	−0.718	0.155	1.760	0.099	0.116	−73.4	MS
NGC 288-063	13.22098	−26.52956	19.15	0.44	−0.767	0.159	1.748	0.100	0.068	−69.3	MS
NGC 288-064	13.24339	−26.58277	19.20	0.47	−0.603	0.176	1.735	0.110	0.233	−77.8	MS

Table A.1. continued.

Id	α(2000)	δ(2000)	V	$B-V$	CN	dCN	CH	dCH	δCN	$v_{\rm rad}$	Type
NGC 288-065	13.22389	−26.53966	19.20	0.43	−0.818	0.157	1.898	0.102	0.018	−65.4	MS
NGC 288-066	13.23320	−26.56424	19.22	0.44	−0.489	0.179	1.662	0.108	0.347	−70.8	MS
NGC 288-067	13.22107	−26.54135	19.25	0.46	−0.781	0.178	1.706	0.110	0.056	−77.0	MS
NGC 288-068	13.22107	−26.54135	19.25	0.46	−0.781	0.178	1.706	0.110	0.056	−77.0	MS
NGC 288-069	13.24484	−26.57078	19.28	0.47	−0.726	0.188	1.756	0.116	0.111	−73.8	MS
NGC 288-070	13.24921	−26.61144	19.36	0.43	−0.514	0.181	1.679	0.113	0.325	−66.8	MS
NGC 288-071	13.22695	−26.54334	19.39	0.46	−0.589	0.176	1.725	0.111	0.250	−72.6	MS
NGC 288-072	13.24306	−26.55599	19.39	0.49	−0.708	0.179	1.801	0.116	0.131	−73.1	MS
NGC 288-073	13.24092	−26.63545	19.41	0.46	−0.529	0.173	1.679	0.114	0.310	−70.8	MS
NGC 288-074	13.22211	−26.54883	19.50	0.47	−0.621	0.193	1.796	0.121	0.219	−74.4	MS
NGC 288-075	13.24784	−26.59811	19.50	0.42	−0.478	0.207	1.638	0.132	0.362	−64.4	MS
NGC 288-076	13.23084	−26.52602	19.54	0.47	−0.634	0.195	1.660	0.123	0.208	−76.0	MS
NGC 288-077	13.23209	−26.56299	19.60	0.49	−0.575	0.208	1.706	0.129	0.268	−71.5	MS
NGC 288-078	13.23842	−26.53609	19.62	0.47	−0.566	0.223	1.714	0.134	0.277	−78.8	MS
NGC 288-079	13.25103	−26.63716	19.63	0.45	0.345	0.200	1.712	0.125	1.188	−81.5	MS
NGC 288-080	13.24588	−26.62907	19.64	0.46	−0.484	0.197	1.684	0.124	0.359	−64.9	MS
NGC 288-081	13.23252	−26.59295	19.65	0.51	−0.900	0.205	1.768	0.131	−0.057	−72.9	MS
NGC 288-082	13.24570	−26.57643	19.67	0.50	−0.664	0.219	1.744	0.136	0.179	−62.5	MS
NGC 288-083	13.24579	−26.62047	19.68	0.47	−0.539	0.199	1.653	0.128	0.305	−72.5	MS
NGC 288-084	13.23610	−26.61677	19.68	0.48	−0.756	0.209	1.682	0.133	0.087	−72.9	MS
NGC 288-085	13.24088	−26.55429	19.69	0.50	−0.719	0.211	1.774	0.135	0.125	−68.4	MS
NGC 288-086	13.23434	−26.56785	19.70	0.50	−0.623	0.214	1.801	0.135	0.221	−68.1	MS
NGC 288-087	13.23430	−26.57322	19.72	0.59	−0.700	0.228	1.911	0.144	0.144	−61.6	MS
NGC 288-088	13.22683	−26.55220	19.74	0.49	−0.809	0.236	1.884	0.152	0.036	−61.8	MS
NGC 288-089	13.23172	−26.56124	19.74	0.48	−0.319	0.240	1.753	0.145	0.526	−75.8	MS
NGC 288-090	13.25343	−26.61468	19.77	0.47	−0.609	0.229	1.889	0.150	0.236	−90.5	MS
NGC 288-091	13.24805	−26.62451	19.83	0.49	−0.641	0.250	1.678	0.150	0.205	−67.3	MS
NGC 288-092	13.23631	−26.52126	19.95	0.52	−0.551	0.268	1.847	0.171	0.298	−78.1	MS
NGC 288-093	13.24568	−26.61894	19.97	0.49	−0.570	0.236	1.796	0.153	0.278	−79.9	MS
NGC 288-094	13.24649	−26.62229	19.98	0.50	−0.515	0.263	1.841	0.166	0.334	−73.6	MS
NGC 288-095	13.23555	−26.55945	19.99	0.56	−0.755	0.262	1.898	0.164	0.094	−59.4	MS
NGC 288-096	13.25435	−26.56649	20.13	0.54	−0.560	0.279	1.852	0.175	0.291	−72.1	MS
NGC 288-097	13.24945	−26.59090	20.14	0.49	−0.664	0.243	1.848	0.162	0.187	−66.2	MS
NGC 288-098	13.24945	−26.59090	20.19	0.52	−0.523	0.244	1.906	0.159	0.329	−63.1	MS
NGC 288-099	13.24487	−26.53475	20.19	0.50	−0.726	0.318	1.793	0.187	0.126	−74.1	MS
NGC 362-001	15.70094	−70.86414	16.73	0.81	−0.051	0.066	2.115	0.039	0.822	219.7	RGB
NGC 362-002	15.62026	−70.90492	16.74	0.80	−0.648	0.064	2.243	0.040	0.225	202.7	RGB
NGC 362-003	15.70814	−70.83189	16.92	0.79	−0.720	0.071	2.193	0.044	0.154	221.1	RGB
NGC 362-004	15.69642	−70.87922	17.03	0.78	−0.525	0.072	2.153	0.046	0.350	206.1	RGB
NGC 362-005	15.73940	−70.84594	17.18	0.80	0.115	0.087	2.081	0.049	0.990	199.7	RGB
NGC 362-006	15.65438	−70.87340	17.40	0.73	−0.009	0.087	2.058	0.051	0.868	208.8	RGB
NGC 362-007	15.68017	−70.83588	17.50	0.75	−0.774	0.090	2.206	0.057	0.104	229.3	RGB
NGC 362-008	15.64375	−70.87226	17.54	0.74	−0.673	0.089	2.218	0.056	0.205	220.5	RGB
NGC 362-009	15.68763	−70.81459	17.59	0.74	−0.075	0.097	2.109	0.057	0.803	217.2	RGB
NGC 362-010	15.64325	−70.84042	17.64	0.73	−0.243	0.098	2.070	0.059	0.636	219.1	RGB
NGC 362-011	15.69340	−70.86878	17.76	0.75	−0.727	0.094	2.209	0.064	0.153	203.4	RGB
NGC 362-012	15.66295	−70.82199	17.88	0.71	−0.150	0.107	1.985	0.063	0.731	219.6	RGB
NGC 362-013	15.65115	−70.89311	17.91	0.70	−0.235	0.107	2.048	0.065	0.646	202.6	RGB
NGC 362-014	15.62802	−70.82859	18.10	0.70	−0.780	0.116	2.130	0.073	0.102	215.7	RGB
NGC 362-015	15.72177	−70.85894	18.15	0.68	−0.813	0.115	2.100	0.075	0.070	216.1	RGB
NGC 362-016	15.61183	−70.89585	18.19	0.67	−0.254	0.119	2.085	0.072	0.629	213.2	RGB
NGC 362-017	15.69619	−70.83124	18.19	0.67	−0.314	0.124	1.985	0.075	0.569	226.5	RGB
NGC 362-018	15.71288	−70.81831	18.25	0.66	−0.258	0.118	1.943	0.073	0.626	211.9	RGB
NGC 362-019	15.71934	−70.83878	18.26	0.65	−0.187	0.124	1.897	0.075	0.697	207.4	RGB
NGC 362-020	15.72946	−70.88968	18.27	0.66	−0.763	0.114	2.021	0.075	0.121	208.2	RGB
NGC 362-021	15.71244	−70.86155	18.30	0.60	−0.642	0.106	1.849	0.070	0.242	219.7	SGB
NGC 362-022	15.68541	−70.86013	18.30	0.61	−0.791	0.110	2.003	0.074	0.093	215.6	SGB
NGC 362-023	15.61372	−70.88400	18.31	0.58	−0.851	0.111	2.026	0.073	0.033	218.4	SGB
NGC 362-024	15.66226	−70.79932	18.32	0.53	−0.723	0.108	1.773	0.071	0.161	235.4	SGB
NGC 362-025	15.61367	−70.81248	18.33	0.57	−0.369	0.110	1.817	0.070	0.515	224.2	SGB
NGC 362-026	15.69106	−70.88836	18.34	0.52	−0.756	0.109	1.793	0.073	0.128	208.3	SGB

Table A.1. continued.

Id	α(2000)	δ(2000)	V	$B-V$	CN	dCN	CH	dCH	δCN	$v_{\rm rad}$	Type
NGC 362-027	15.65406	−70.82763	18.34	0.55	−0.751	0.112	1.875	0.072	0.133	219.3	SGB
NGC 362-028	15.64568	−70.80231	18.35	0.54	−0.829	0.110	1.887	0.072	0.056	217.7	SGB
NGC 362-029	15.60575	−70.83384	18.36	0.54	−0.519	0.109	1.799	0.069	0.366	225.4	SGB
NGC 362-030	15.68082	−70.82403	18.37	0.54	−0.637	0.111	1.704	0.071	0.247	218.2	SGB
NGC 362-031	15.64068	−70.89159	18.37	0.51	−0.558	0.107	1.773	0.070	0.326	212.9	SGB
NGC 362-032	15.73449	−70.81566	18.38	0.53	−0.768	0.113	1.762	0.074	0.117	215.3	SGB
NGC 362-033	15.70773	−70.85012	18.38	0.50	−0.705	0.111	1.796	0.072	0.180	231.0	SGB
NGC 362-034	15.71192	−70.82009	18.39	0.51	−0.555	0.110	1.733	0.073	0.330	204.2	SGB
NGC 362-035	15.63085	−70.88231	18.39	0.48	−0.756	0.115	1.739	0.075	0.129	210.1	SGB
NGC 362-036	15.59876	−70.80515	18.40	0.52	−0.669	0.108	1.742	0.071	0.216	230.2	SGB
NGC 362-037	15.69928	−70.84210	18.40	0.60	−0.592	0.112	1.871	0.073	0.292	227.2	SGB
NGC 362-038	15.62638	−70.84452	18.40	0.51	−0.733	0.116	1.695	0.071	0.152	218.4	SGB
NGC 362-039	15.63059	−70.80403	18.41	0.50	−0.694	0.112	1.762	0.072	0.191	225.9	SGB
NGC 362-040	15.68510	−70.87556	18.41	0.51	−0.608	0.112	1.724	0.074	0.277	207.1	SGB
NGC 362-041	15.68500	−70.86633	18.42	0.51	−0.674	0.106	1.660	0.071	0.211	216.9	SGB
NGC 362-042	15.65406	−70.89685	18.57	0.50	−0.683	0.114	1.813	0.076	0.203	227.4	SGB
NGC 362-043	15.67477	−70.90345	18.89	0.44	−0.940	0.173	1.690	0.114	−0.052	241.3	MS
NGC 362-044	15.63644	−70.84245	18.89	0.42	−0.826	0.213	1.708	0.135	0.062	237.4	MS
NGC 362-045	15.69096	−70.85859	18.90	0.42	−0.698	0.185	1.617	0.121	0.190	245.7	MS
NGC 362-046	15.65185	−70.80303	18.91	0.42	−0.814	0.216	1.750	0.140	0.074	256.5	MS
NGC 362-047	15.65667	−70.84093	18.92	0.47	−0.871	0.194	1.711	0.127	0.017	256.7	MS
NGC 362-048	15.71316	−70.80703	18.92	0.44	−0.616	0.189	1.668	0.123	0.272	266.7	MS
NGC 362-049	15.67617	−70.87918	18.92	0.40	−0.818	0.192	1.697	0.126	0.070	244.5	MS
NGC 362-050	15.66321	−70.85285	18.94	0.47	−0.524	0.209	1.716	0.129	0.365	262.5	MS
NGC 362-051	15.69220	−70.83378	18.97	0.38	−0.627	0.199	1.712	0.128	0.262	257.3	MS
NGC 362-052	15.67105	−70.81799	18.98	0.42	−0.639	0.194	1.684	0.126	0.250	254.5	MS
NGC 362-053	15.65119	−70.86436	19.01	0.42	−0.446	0.185	1.675	0.116	0.443	262.9	MS
NGC 362-054	15.69001	−70.82183	19.06	0.44	−0.737	0.237	1.688	0.154	0.153	267.7	MS
NGC 362-055	15.69821	−70.82019	19.09	0.45	−0.695	0.200	1.651	0.130	0.195	265.2	MS
NGC 362-056	15.68329	−70.83914	19.09	0.46	−0.936	0.223	1.697	0.142	−0.046	241.6	MS
NGC 362-057	15.64778	−70.88107	19.10	0.41	−0.534	0.199	1.704	0.132	0.356	230.3	MS
NGC 362-058	15.71673	−70.80912	19.13	0.46	−0.556	0.199	1.727	0.133	0.334	262.6	MS
NGC 362-059	15.68672	−70.86018	19.15	0.40	−0.690	0.171	1.736	0.113	0.200	258.5	MS
NGC 362-060	15.63856	−70.84953	19.20	0.44	−0.684	0.226	1.639	0.142	0.207	266.8	MS
NGC 362-061	15.70660	−70.84726	19.22	0.49	−0.677	0.256	1.828	0.161	0.214	255.5	MS
NGC 362-062	15.67827	−70.82522	19.22	0.45	−0.650	0.216	1.573	0.137	0.241	239.5	MS
NGC 362-063	15.61550	−70.87506	19.23	0.42	−0.576	0.226	1.731	0.143	0.315	234.0	MS
NGC 362-064	15.67394	−70.89766	19.25	0.44	−0.706	0.209	1.701	0.139	0.185	236.6	MS
NGC 362-065	15.67702	−70.88194	19.26	0.42	−0.661	0.235	1.693	0.151	0.230	256.5	MS
NGC 362-066	15.66786	−70.80237	19.26	0.46	−0.697	0.228	1.658	0.147	0.194	262.3	MS
NGC 362-067	15.68542	−70.87747	19.33	0.45	−0.792	0.279	1.804	0.174	0.099	229.7	MS
NGC 362-068	15.70748	−70.82939	19.34	0.43	−0.650	0.223	1.668	0.146	0.242	257.1	MS
NGC 362-069	15.64197	−70.88671	19.37	0.41	−0.642	0.228	1.810	0.153	0.250	239.1	MS
NGC 362-070	15.66107	−70.89398	19.37	0.47	−0.654	0.215	1.696	0.140	0.238	241.7	MS
NGC 362-071	15.71891	−70.81242	19.43	0.46	−0.735	0.280	1.656	0.183	0.157	260.8	MS
NGC 362-072	15.62668	−70.88534	19.44	0.42	−0.789	0.235	1.735	0.155	0.103	225.4	MS
NGC 362-073	15.64042	−70.85121	19.44	0.47	−0.687	0.257	1.888	0.167	0.205	258.1	MS
NGC 362-074	15.62644	−70.89608	19.52	0.45	−0.800	0.276	1.706	0.172	0.093	233.7	MS
NGC 362-075	15.67252	−70.79427	19.57	0.46	−0.689	0.270	1.618	0.181	0.204	266.7	MS
NGC 362-076	15.68330	−70.81533	19.62	0.47	−0.663	0.274	1.806	0.186	0.231	261.0	MS
NGC 362-077	15.65887	−70.89216	19.84	0.49	−0.712	0.297	1.671	0.185	0.183	213.9	MS
NGC 5286-001	206.54955	−51.42272	16.77	1.08	−0.051	0.099	2.047	0.057	0.741	90.0	RGB
NGC 5286-002	206.54435	−51.40362	16.91	1.07	0.002	0.104	2.183	0.059	0.796	84.1	RGB
NGC 5286-003	206.53143	−51.40539	17.83	0.97	−0.085	0.144	1.884	0.083	0.724	88.7	RGB
NGC 5286-004	206.56119	−51.42629	17.96	1.03	−0.549	0.150	2.049	0.096	0.262	86.2	RGB
NGC 5286-005	206.56752	−51.42112	18.05	0.96	−0.810	0.152	2.141	0.096	0.002	73.4	RGB
NGC 5286-006	206.53137	−51.39231	18.35	0.94	−0.223	0.172	1.830	0.102	0.594	80.4	RGB
NGC 5286-007	206.54788	−51.36254	19.01	0.86	−0.953	0.216	2.071	0.139	−0.126	102.1	SGB
NGC 5286-008	206.53696	−51.33876	19.03	0.83	−0.612	0.209	1.854	0.133	0.216	105.6	SGB
NGC 5286-009	206.55163	−51.39615	19.71	0.68	−0.802	0.216	1.598	0.141	0.036	86.4	SGB
NGC 5286-010	206.53925	−51.34506	19.74	0.79	−0.395	0.298	1.952	0.190	0.444	99.5	SGB
M 22-001	279.02891	−23.91745	15.28	0.79	−0.187	0.066	2.316	0.035	0.483	−125.7	RGB

Table A.1. continued.

Id	α(2000)	δ(2000)	V	$B-V$	CN	dCN	CH	dCH	δCN	$v_{\rm rad}$	Type
M 22-002	279.04091	−23.91550	16.20	0.80	0.096	0.100	1.984	0.052	0.802	−147.9	RGB
M 22-003	279.05050	−23.92792	16.32	0.77	−0.459	0.100	1.908	0.054	0.252	−141.3	RGB
M 22-004	279.05276	−23.92067	16.33	0.79	−0.589	0.099	1.961	0.056	0.122	−132.7	RGB
M 22-005	279.05760	−23.88352	16.38	0.84	0.199	0.098	1.949	0.051	0.913	−136.2	RGB
M 22-006	279.04857	−23.87365	16.38	0.83	−0.536	0.100	1.888	0.055	0.177	−125.1	RGB
M 22-007	279.03108	−23.90537	16.46	0.78	−0.509	0.096	1.953	0.053	0.208	−137.8	RGB
M 22-008	279.05745	−23.87208	16.49	0.79	−0.341	0.114	1.803	0.059	0.377	−136.6	RGB
M 22-009	279.03129	−23.94113	16.58	0.76	−0.636	0.105	1.823	0.058	0.085	−133.7	RGB
M 22-010	279.03517	−23.85592	16.64	0.80	−0.780	0.095	1.947	0.054	−0.056	−118.1	RGB
M 22-011	279.06252	−23.89160	16.67	0.81	−0.119	0.122	1.724	0.063	0.606	−127.0	RGB
M 22-012	279.06206	−23.84654	16.68	0.81	−0.263	0.133	1.838	0.068	0.463	−140.9	RGB
M 22-013	279.05838	−23.85886	16.68	0.80	−0.518	0.111	1.758	0.061	0.207	−127.3	RGB
M 22-014	279.04689	−23.86696	16.71	0.83	−0.083	0.136	2.046	0.070	0.644	−133.4	RGB
M 22-015	279.04205	−23.91396	16.71	0.70	−0.377	0.104	1.692	0.057	0.349	−129.8	SGB
M 22-016	279.06023	−23.90403	16.76	0.72	−0.548	0.104	1.789	0.059	0.181	−121.9	SGB
M 22-017	279.03037	−23.90847	16.79	0.80	−0.663	0.095	1.697	0.056	0.067	−107.0	RGB
M 22-018	279.02381	−23.88081	16.82	0.74	−0.496	0.106	1.735	0.059	0.234	−133.3	SGB
M 22-019	279.04432	−23.89746	16.82	0.69	−0.464	0.101	1.721	0.057	0.267	−118.9	SGB
M 22-020	279.03952	−23.85198	16.82	0.77	−0.631	0.113	1.855	0.062	0.100	−124.2	RGB
M 22-021	279.05528	−23.89469	16.86	0.71	−0.684	0.095	1.715	0.056	0.048	−137.8	SGB
M 22-022	279.04354	−23.92439	16.89	0.70	−0.549	0.106	1.850	0.061	0.185	−135.0	SGB
M 22-023	279.04756	−23.89345	16.93	0.76	−0.191	0.148	2.017	0.078	0.545	−130.1	SGB
M 22-024	279.04237	−23.95182	16.93	0.67	−0.530	0.101	1.807	0.058	0.206	−129.8	SGB
M 22-025	279.04546	−23.94727	16.96	0.73	−0.195	0.112	1.947	0.062	0.541	−133.8	SGB
M 22-026	279.06095	−23.85099	16.96	0.71	−0.453	0.140	1.644	0.074	0.283	−124.5	SGB
M 22-027	279.06098	−23.89917	16.97	0.68	−0.491	0.104	1.662	0.060	0.246	−102.2	SGB
M 22-028	279.04295	−23.89064	16.97	0.74	−0.267	0.126	1.799	0.068	0.470	−135.2	SGB
M 22-029	279.03779	−23.88544	16.99	0.66	−0.461	0.114	1.747	0.065	0.277	−134.6	SGB
M 22-030	279.05715	−23.86118	17.01	0.63	−0.615	0.115	1.735	0.066	0.123	−110.5	SGB
M 22-031	279.05047	−23.85347	17.03	0.68	−0.560	0.118	1.695	0.066	0.179	−116.0	SGB
M 22-032	279.06222	−23.87841	17.05	0.75	−0.395	0.141	1.641	0.073	0.345	−135.0	SGB
M 22-033	279.03841	−23.87661	17.06	0.64	−0.637	0.115	1.698	0.064	0.103	−110.5	SGB
M 22-034	279.04397	−23.95963	17.10	0.61	−0.667	0.099	1.619	0.060	0.075	−129.7	SGB
M 22-035	279.05138	−23.90741	17.10	0.63	−0.630	0.109	1.648	0.062	0.112	−114.0	SGB
M 22-036	279.04397	−23.95963	17.10	0.61	−0.667	0.099	1.619	0.060	0.075	−129.7	SGB
M 22-037	279.03706	−23.90174	17.11	0.64	−0.752	0.128	1.559	0.072	−0.010	−128.6	SGB
M 22-038	279.05045	−23.95082	17.11	0.61	−0.570	0.100	1.703	0.060	0.172	−132.8	SGB
M 22-039	279.03991	−23.94901	17.11	0.66	−0.512	0.111	1.698	0.063	0.230	−136.4	SGB
M 22-040	279.05344	−23.96111	17.12	0.65	−0.313	0.119	1.710	0.065	0.430	−141.9	SGB
M 22-041	279.04552	−23.93060	17.12	0.61	−0.597	0.139	1.683	0.075	0.146	−122.6	SGB
M 22-042	279.03936	−23.92582	17.17	0.59	−0.480	0.129	1.692	0.073	0.265	−135.3	SGB
M 22-043	279.04863	−23.86465	17.20	0.64	−0.328	0.124	1.669	0.068	0.418	−113.5	SGB
M 22-044	279.05992	−23.84805	17.21	0.66	−0.535	0.138	1.667	0.077	0.211	−114.6	SGB
M 22-045	279.05043	−23.88240	17.21	0.66	−0.473	0.145	1.724	0.077	0.273	−135.5	SGB
M 22-046	279.04350	−23.91890	17.22	0.63	−0.778	0.137	1.771	0.077	−0.031	−139.5	SGB
M 22-047	279.06073	−23.87510	17.23	0.63	−0.495	0.125	1.555	0.071	0.252	−130.1	SGB
M 22-048	279.04008	−23.93242	17.24	0.64	−0.554	0.128	1.726	0.071	0.193	−129.7	SGB
M 22-049	279.05270	−23.86817	17.25	0.65	−0.581	0.119	1.673	0.067	0.167	−112.3	SGB
M 22-050	279.03700	−23.87038	17.27	0.68	−0.535	0.141	1.739	0.077	0.213	−116.7	SGB
M 22-051	279.05241	−23.90052	17.28	0.63	−0.485	0.129	1.738	0.073	0.264	−119.2	SGB
M 22-052	279.04862	−23.93754	17.29	0.59	−0.664	0.132	1.665	0.072	0.085	−136.6	SGB
M 22-053	279.04353	−23.86241	17.34	0.64	−0.476	0.138	1.734	0.077	0.275	−123.3	SGB
M 22-054	279.05475	−23.88720	17.39	0.56	−0.547	0.126	1.635	0.071	0.207	−112.6	SGB
M 22-055	279.05890	−23.87640	17.51	0.65	−0.477	0.126	1.599	0.077	0.281	−96.9	MS
M 22-056	279.04447	−23.92742	17.55	0.63	−0.695	0.126	1.631	0.077	0.065	−125.2	MS
M 22-057	279.06106	−23.85731	17.57	0.60	−0.430	0.125	1.601	0.079	0.330	−96.7	MS
M 22-058	279.03079	−23.92864	17.57	0.58	−0.635	0.125	1.640	0.077	0.125	−142.6	MS
M 22-059	279.03416	−23.93864	17.62	0.60	−0.680	0.137	1.608	0.084	0.082	−115.7	MS
M 22-060	279.03410	−23.88717	17.63	0.62	−0.875	0.118	1.602	0.072	−0.112	−90.5	MS
M 22-061	279.02809	−23.92253	17.63	0.58	−0.653	0.143	1.759	0.087	0.110	−132.6	MS
M 22-062	279.04247	−23.91618	17.64	0.57	−0.566	0.119	1.587	0.071	0.197	−121.9	MS
M 22-063	279.04189	−23.96029	17.65	0.62	−0.605	0.117	1.708	0.074	0.159	−123.7	MS

Table A.1. continued.

Id	α(2000)	δ(2000)	V	$B-V$	CN	dCN	CH	dCH	δCN	$v_{\rm rad}$	Type
M 22-064	279.02423	−23.90893	17.69	0.61	−0.507	0.134	1.628	0.081	0.258	−112.8	MS
M 22-065	279.03155	−23.93055	17.71	0.56	−0.653	0.141	1.662	0.088	0.113	−124.5	MS
M 22-066	279.05005	−23.90834	17.86	0.60	−0.659	0.128	1.343	0.080	0.113	−94.6	MS
M 22-067	279.04560	−23.86954	17.87	0.69	−0.614	0.149	1.660	0.087	0.159	−111.2	MS
M 22-068	279.04857	−23.92098	17.89	0.64	−0.623	0.147	1.729	0.088	0.150	−98.8	MS
M 22-069	279.03686	−23.89126	17.90	0.54	−0.843	0.127	1.603	0.080	−0.069	−105.5	MS
M 22-070	279.05969	−23.86506	17.91	0.65	−0.627	0.168	1.564	0.100	0.147	−97.7	MS
M 22-071	279.04780	−23.90671	17.91	0.68	−0.759	0.153	1.646	0.094	0.015	−125.5	MS
M 22-072	279.03362	−23.93664	17.96	0.60	−0.555	0.144	1.675	0.087	0.221	−117.7	MS
M 22-073	279.03367	−23.93484	17.98	0.57	−0.498	0.144	1.596	0.091	0.279	−113.1	MS
M 22-074	279.03709	−23.94155	17.98	0.66	−0.530	0.076	1.680	0.049	0.247	−102.7	MS
M 22-075	279.05259	−23.93333	18.01	0.62	−0.448	0.136	1.662	0.083	0.330	−124.0	MS
M 22-076	279.04092	−23.87893	18.04	0.69	−0.706	0.166	1.823	0.105	0.073	−113.7	MS
M 22-077	279.04153	−23.88500	18.05	0.65	−0.424	0.155	1.716	0.091	0.355	−111.9	MS
M 22-078	279.05215	−23.89776	18.05	0.67	−0.736	0.196	1.635	0.119	0.043	−124.2	MS
M 22-079	279.03621	−23.92610	18.06	0.56	−0.627	0.162	1.603	0.101	0.153	−111.6	MS
M 22-080	279.05975	−23.88213	18.06	0.70	−0.528	0.143	1.589	0.091	0.252	−102.4	MS
M 22-081	279.04965	−23.90096	18.20	0.65	−0.855	0.176	1.561	0.110	−0.069	−106.3	MS
M 22-082	279.05433	−23.86839	18.22	0.66	−0.603	0.203	1.450	0.116	0.184	−128.3	MS
M 22-083	279.05075	−23.85956	18.23	0.67	−0.530	0.199	1.628	0.119	0.257	−110.3	MS
M 22-084	279.05851	−23.86318	18.25	0.67	−0.676	0.211	1.493	0.129	0.111	−143.0	MS
M 22-085	279.05880	−23.86156	18.26	0.69	−0.387	0.176	1.554	0.109	0.401	−102.5	MS
M 22-086	279.06292	−23.87166	18.37	0.66	−0.439	0.187	1.710	0.110	0.353	−104.8	MS
M 22-087	279.04513	−23.89536	18.40	0.69	−0.364	0.201	1.576	0.121	0.429	−111.9	MS
M 22-088	279.03918	−23.95704	18.40	0.66	−0.445	0.176	1.828	0.111	0.349	−122.7	MS
M 22-089	279.03175	−23.91428	18.43	0.61	−0.729	0.192	1.672	0.122	0.065	−136.7	MS
M 22-090	279.02337	−23.89604	18.43	0.68	−0.333	0.206	1.671	0.122	0.461	−130.3	MS
M 22-091	279.05090	−23.93196	18.52	0.66	−0.687	0.216	1.667	0.130	0.111	−115.5	MS
M 22-092	279.05259	−23.85861	18.54	0.73	−0.721	0.171	1.658	0.103	0.078	−106.7	MS
M 22-093	279.04368	−23.95893	18.59	0.62	−0.841	0.187	1.476	0.115	−0.040	−130.2	MS
M 22-094	279.04368	−23.95893	18.59	0.62	−0.841	0.187	1.476	0.115	−0.040	−130.2	MS
M 22-095	279.03898	−23.95518	18.60	0.66	−0.612	0.137	1.809	0.091	0.189	−96.8	MS
M 22-096	279.05470	−23.95105	18.72	0.70	−0.453	0.196	1.802	0.123	0.353	−141.5	MS
M 22-097	279.04649	−23.88956	18.73	0.74	−0.433	0.198	1.739	0.117	0.373	−116.8	MS
Ter7-001	289.40929	−34.65456	16.82	1.22	0.350	0.129	2.425	0.054	0.396	125.9	RGB
Ter7-002	289.43408	−34.67519	16.95	1.19	0.050	0.128	2.366	0.057	0.128	139.2	RGB
Ter7-003	289.44845	−34.65597	17.42	1.08	0.179	0.152	2.412	0.069	0.371	138.5	RGB
Ter7-004	289.44580	−34.64778	17.51	1.10	0.147	0.145	2.399	0.070	0.361	147.0	RGB
Ter7-005	289.41804	−34.68052	17.53	0.98	−0.265	0.119	2.304	0.065	−0.046	138.1	RGB
Ter7-006	289.40815	−34.63017	17.81	0.90	−0.311	0.121	2.279	0.068	−0.025	132.3	HB
Ter7-007	289.41169	−34.66350	17.81	0.88	−0.157	0.126	2.265	0.070	0.130	134.9	HB
Ter7-008	289.45129	−34.67602	17.85	1.07	−0.024	0.163	2.327	0.083	0.274	124.5	RGB
Ter7-009	289.44594	−34.68272	17.88	1.02	0.051	0.159	2.377	0.082	0.356	129.9	RGB
Ter7-010	289.41642	−34.66780	18.05	1.05	−0.198	0.164	2.459	0.087	0.148	130.3	RGB
Ter7-011	289.42025	−34.65818	18.06	1.00	−0.306	0.163	2.391	0.085	0.042	136.7	RGB
Ter7-012	289.45472	−34.60692	18.18	0.99	0.066	0.168	2.366	0.087	0.444	123.0	RGB
Ter7-013	289.43835	−34.69527	18.27	0.95	−0.140	0.191	2.286	0.096	0.261	121.4	RGB
Ter7-014	289.44562	−34.65256	18.30	0.97	−0.119	0.178	2.418	0.095	0.287	133.4	RGB
Ter7-015	289.44512	−34.67927	18.34	1.03	−0.068	0.187	2.301	0.099	0.348	127.9	RGB
Ter7-016	289.42479	−34.66234	18.43	0.89	−0.426	0.170	2.343	0.095	0.011	143.2	RGB
Ter7-017	289.41509	−34.64859	18.71	0.95	−0.275	0.212	2.366	0.111	0.233	139.2	RGB
Ter7-018	289.43972	−34.64429	18.90	0.88	−0.558	0.218	2.357	0.119	−0.005	131.9	RGB
Ter7-019	289.43300	−34.64258	18.93	0.93	−0.135	0.215	2.322	0.120	0.426	147.2	RGB
Ter7-020	289.39695	−34.61736	19.04	0.91	−0.347	0.215	2.437	0.126	0.241	141.3	RGB
Ter7-021	289.41505	−34.66078	19.23	0.88	−0.435	0.250	2.379	0.140	0.199	138.7	RGB
Ter7-022	289.43115	−34.65116	19.34	0.86	−0.263	0.243	2.293	0.142	0.397	146.5	RGB
Ter7-023	289.42779	−34.65015	19.83	0.84	−0.640	0.308	2.296	0.184	0.140	135.2	RGB
Ter7-024	289.40900	−34.69272	20.18	0.80	−0.597	0.345	2.378	0.205	0.268	156.9	SGB
Ter7-025	289.40196	−34.62030	20.24	0.83	−0.714	0.335	2.274	0.211	0.165	160.5	SGB
Ter7-026	289.42344	−34.64369	20.35	0.84	−0.576	0.386	2.215	0.236	0.332	174.4	SGB
Ter7-027	289.42625	−34.63302	20.40	0.76	−0.536	0.345	2.328	0.217	0.383	160.5	SGB
Ter7-028	289.40478	−34.67403	20.42	0.65	−0.413	0.313	2.024	0.202	0.510	178.4	SGB
Ter7-029	289.40421	−34.67166	20.42	0.64	−0.756	0.297	2.055	0.195	0.167	165.4	SGB

Table A.1. continued.

Id	α(2000)	δ(2000)	V	$B-V$	CN	dCN	CH	dCH	δCN	$v_{\rm rad}$	Type
Ter7-030	289.43229	−34.64281	20.44	0.69	−0.707	0.371	2.157	0.229	0.223	161.0	SGB
Ter7-031	289.42343	−34.69758	20.45	0.55	−0.699	0.303	1.921	0.201	0.232	161.0	SGB
Ter7-032	289.44575	−34.62801	20.46	0.57	−0.819	0.278	1.806	0.190	0.114	136.5	SGB
Ter7-033	289.40126	−34.63623	20.48	0.73	−0.842	0.347	2.349	0.221	0.098	159.6	SGB
Ter7-034	289.40368	−34.63776	20.49	0.56	−0.786	0.279	1.887	0.192	0.157	159.4	SGB
Ter7-035	289.45130	−34.70464	20.49	0.52	−0.930	0.289	2.106	0.198	0.012	160.2	SGB
Ter7-036	289.41663	−34.62640	20.52	0.56	−0.846	0.284	1.848	0.185	0.102	162.7	SGB
Ter7-037	289.43176	−34.62916	20.52	0.53	−0.816	0.282	1.918	0.189	0.132	179.1	SGB
Ter7-038	289.42994	−34.66954	20.52	0.56	−0.626	0.301	1.875	0.201	0.323	160.7	SGB
Ter7-039	289.43507	−34.68520	20.52	0.53	−0.911	0.288	1.789	0.191	0.037	149.0	SGB
Ter7-040	289.43759	−34.66819	20.53	0.54	−0.834	0.303	1.669	0.194	0.119	151.0	SGB
Ter7-041	289.45039	−34.63995	20.53	0.48	−0.606	0.277	1.748	0.184	0.344	176.0	SGB
Ter7-042	289.43982	−34.67093	20.54	0.55	−0.903	0.293	1.740	0.197	0.051	149.5	SGB
Ter7-043	289.43235	−34.64992	20.55	0.55	−0.944	0.296	1.898	0.197	0.011	177.9	SGB
Ter7-044	289.44499	−34.67294	20.55	0.53	−0.953	0.311	1.747	0.205	0.003	148.0	SGB
Ter7-045	289.42663	−34.65049	20.56	0.57	−0.877	0.327	1.773	0.217	0.081	164.0	SGB
Ter7-046	289.43079	−34.64511	20.57	0.53	−0.607	0.293	1.812	0.199	0.354	175.9	SGB
Ter7-047	289.45466	−34.62447	20.58	0.58	−0.578	0.316	1.879	0.201	0.386	164.1	SGB
M 15-001	322.52784	12.19498	17.17	0.72	−0.459	0.093	1.695	0.057	0.278	−128.5	RGB
M 15-002	322.56545	12.21040	17.51	0.71	−0.553	0.105	1.659	0.066	0.188	−128.7	RGB
M 15-003	322.53617	12.13113	17.52	0.67	−0.598	0.097	1.751	0.064	0.143	−98.6	RGB
M 15-004	322.53279	12.18582	17.55	0.71	−0.718	0.111	1.740	0.070	0.023	−111.0	RGB
M 15-005	322.54196	12.15207	17.61	0.67	−0.670	0.113	1.729	0.072	0.072	−107.7	RGB
M 15-006	322.53398	12.11966	17.72	0.68	−0.658	0.110	1.866	0.072	0.085	−97.5	RGB
M 15-007	322.53916	12.11189	17.81	0.68	−0.669	0.115	1.819	0.075	0.075	−112.6	RGB
M 15-008	322.55596	12.14574	17.82	0.72	0.406	0.135	2.226	0.082	1.150	−113.8	RGB
M 15-009	322.51785	12.20575	17.86	0.68	−0.763	0.119	1.796	0.077	−0.018	−116.4	RGB
M 15-010	322.51622	12.11409	17.88	0.67	−0.637	0.115	1.779	0.075	0.108	−94.8	RGB
M 15-011	322.53050	12.15494	17.91	0.67	−0.667	0.120	1.679	0.077	0.078	−119.5	RGB
M 15-012	322.55420	12.16274	17.96	0.69	−0.530	0.132	1.679	0.084	0.216	−128.7	RGB
M 15-013	322.53932	12.19168	17.97	0.68	−0.689	0.130	1.757	0.083	0.057	−105.5	RGB
M 15-014	322.55938	12.13849	18.08	0.64	−0.680	0.124	1.729	0.082	0.067	−114.4	RGB
M 15-015	322.52163	12.20011	18.14	0.66	−0.288	0.148	1.777	0.093	0.460	−114.9	RGB
M 15-016	322.52709	12.18998	18.18	0.66	−0.732	0.136	1.704	0.086	0.016	−123.2	RGB
M 15-017	322.55024	12.17514	18.24	0.67	−0.571	0.145	1.662	0.093	0.178	−119.2	RGB
M 15-018	322.53782	12.18791	18.26	0.67	−0.697	0.143	1.718	0.091	0.052	−116.4	RGB
M 15-019	322.54437	12.21514	18.33	0.63	−0.484	0.144	1.648	0.093	0.266	−128.0	RGB
M 15-020	322.53777	12.11650	18.40	0.59	−0.600	0.142	1.644	0.093	0.150	−105.4	SGB
M 15-021	322.53631	12.13532	18.46	0.58	−0.463	0.144	1.670	0.095	0.288	−114.3	SGB
M 15-022	322.53770	12.14231	18.51	0.56	−0.473	0.145	1.543	0.095	0.279	−117.4	SGB
M 15-023	322.54808	12.19635	18.52	0.58	−0.587	0.157	1.661	0.101	0.165	−112.1	SGB
M 15-024	322.54320	12.20758	18.53	0.55	−0.487	0.149	1.578	0.099	0.265	−126.0	SGB
M 15-025	322.56614	12.18396	18.54	0.60	−0.518	0.164	1.641	0.105	0.234	−121.7	SGB
M 15-026	322.54833	12.16928	18.54	0.60	−0.659	0.163	1.622	0.106	0.093	−97.2	SGB
M 15-027	322.54058	12.12169	18.55	0.55	−0.646	0.149	1.646	0.097	0.106	−100.9	SGB
M 15-028	322.51466	12.12566	18.56	0.55	−0.673	0.145	1.653	0.096	0.079	−100.8	SGB
M 15-029	322.54464	12.18175	18.59	0.57	−0.692	0.163	1.524	0.104	0.060	−109.1	SGB
M 15-030	322.54177	12.21635	18.60	0.56	−0.584	0.151	1.547	0.099	0.169	−113.3	SGB
M 15-031	322.54845	12.18311	18.63	0.57	−0.671	0.164	1.609	0.103	0.082	−112.8	SGB
M 15-032	322.55170	12.12845	18.64	0.50	−0.560	0.149	1.541	0.098	0.193	−105.3	SGB
M 15-033	322.53302	12.15669	18.66	0.54	−0.543	0.153	1.559	0.101	0.210	−93.1	SGB
M 15-034	322.54343	12.14858	18.67	0.54	−0.717	0.165	1.655	0.107	0.036	−104.5	SGB
M 15-035	322.55392	12.19383	18.69	0.58	−0.692	0.167	1.633	0.110	0.061	−118.2	SGB
M 15-036	322.52440	12.14973	18.70	0.50	−0.776	0.147	1.747	0.093	−0.022	−104.3	SGB
M 15-037	322.54778	12.20403	18.73	0.53	−0.501	0.160	1.625	0.108	0.253	−99.5	SGB
M 15-038	322.55914	12.17986	18.73	0.55	−0.523	0.166	1.551	0.108	0.231	−95.7	SGB
M 15-039	322.52602	12.20912	18.74	0.53	−0.463	0.166	1.488	0.106	0.291	−109.6	SGB
M 15-040	322.52675	12.15351	18.74	0.55	−0.812	0.162	1.636	0.106	−0.058	−108.0	SGB
M 15-041	322.52690	12.22016	18.75	0.49	−0.568	0.159	1.542	0.102	0.186	−98.4	SGB
M 15-042	322.54846	12.16648	18.77	0.53	−0.569	0.176	1.606	0.113	0.185	−105.8	SGB
M 15-043	322.53786	12.17810	18.77	0.54	−0.711	0.169	1.562	0.112	0.044	−94.2	SGB

Table A.1. continued.

Id	α(2000)	δ(2000)	V	$B-V$	CN	dCN	CH	dCH	δCN	$v_{\rm rad}$	Type
M 15-044	322.53134	12.14044	18.81	0.45	−0.751	0.161	1.664	0.107	0.004	−96.5	MS
M 15-045	322.55098	12.12310	18.93	0.46	−0.636	0.168	1.551	0.112	0.120	−95.2	MS
M 15-046	322.53416	12.22428	19.03	0.47	−0.789	0.187	1.598	0.121	−0.032	−112.1	MS
M 15-047	322.54493	12.13650	19.11	0.44	−0.758	0.179	1.583	0.119	0.000	−98.4	MS
M 15-048	322.56599	12.17154	19.14	0.50	−0.604	0.201	1.522	0.129	0.154	−104.0	MS
M 15-049	322.54341	12.22215	19.16	0.40	−0.551	0.192	1.522	0.122	0.207	−97.7	MS
M 15-050	322.56476	12.21860	19.18	0.49	−0.487	0.198	1.566	0.126	0.272	−123.3	MS
M 15-051	322.53418	12.11048	19.19	0.44	−0.680	0.186	1.575	0.124	0.079	−87.8	MS
M 15-052	322.51745	12.13259	19.22	0.44	−0.536	0.197	1.607	0.127	0.223	−96.2	MS
M 15-053	322.54789	12.11769	19.27	0.43	−0.590	0.185	1.569	0.126	0.170	−89.0	MS
M 15-054	322.55332	12.19854	19.28	0.47	−0.612	0.207	1.602	0.138	0.148	−111.4	MS
M 15-055	322.55024	12.12708	19.30	0.43	−0.735	0.206	1.499	0.134	0.025	−88.1	MS
M 15-056	322.55543	12.10858	19.34	0.45	−0.560	0.217	1.559	0.134	0.200	−92.5	MS
M 15-057	322.55270	12.20177	19.51	0.45	−0.780	0.236	1.606	0.153	−0.018	−108.5	MS
Pal12-001	326.66154	−21.24816	16.21	0.90	−0.197	0.100	2.273	0.052	0.227	−5.7	RGB
Pal12-002	326.66939	−21.23127	16.61	0.88	0.151	0.105	2.509	0.057	0.627	8.5	RGB
Pal12-003	326.65155	−21.24316	16.88	0.79	−0.578	0.108	2.208	0.062	−0.068	14.0	HB
Pal12-004	326.67071	−21.25261	16.92	0.75	−0.442	0.094	2.121	0.056	0.073	18.5	HB
Pal12-005	326.67863	−21.26354	16.97	0.74	−0.567	0.095	2.068	0.058	−0.045	17.5	HB
Pal12-006	326.65697	−21.24051	17.01	0.74	−0.403	0.101	2.121	0.059	0.123	7.6	HB
Pal12-007	326.65288	−21.22877	17.02	0.75	−0.540	0.114	2.178	0.064	−0.012	1.2	HB
Pal12-008	326.65937	−21.20296	17.12	0.90	−0.283	0.127	2.347	0.069	0.258	−3.2	RGB
Pal12-009	326.65128	−21.25646	17.15	0.91	−0.363	0.125	2.383	0.069	0.182	17.7	RGB
Pal12-010	326.64049	−21.22997	17.16	0.90	−0.270	0.129	2.332	0.070	0.276	13.7	RGB
Pal12-011	326.64705	−21.25434	17.49	0.87	−0.461	0.148	2.407	0.083	0.127	24.6	RGB
Pal12-012	326.65240	−21.25516	17.56	0.86	−0.180	0.152	2.361	0.086	0.417	26.7	RGB
Pal12-013	326.64743	−21.24233	17.94	0.83	−0.655	0.174	2.288	0.098	−0.009	23.8	RGB
Pal12-014	326.63603	−21.20655	18.23	0.79	−0.387	0.185	2.398	0.108	0.296	−3.9	RGB
Pal12-015	326.65325	−21.29261	18.50	0.75	−0.302	0.192	2.315	0.117	0.415	26.1	RGB
Pal12-016	326.67134	−21.23422	18.67	0.76	−0.542	0.239	2.277	0.142	0.196	2.1	RGB
Pal12-017	326.65305	−21.19291	18.70	0.75	−0.708	0.231	2.343	0.141	0.034	5.2	RGB
Pal12-018	326.64222	−21.29505	18.72	0.93	−0.225	0.307	2.367	0.146	0.520	−4.6	RGB
Pal12-019	326.65428	−21.23765	18.84	0.76	−0.548	0.261	2.335	0.158	0.213	−1.1	RGB
Pal12-020	326.68273	−21.26678	19.00	0.75	−0.764	0.279	2.357	0.171	0.018	17.1	RGB
Pal12-021	326.65948	−21.26204	19.05	0.72	−0.467	0.275	2.209	0.160	0.320	16.7	RGB
Pal12-022	326.65316	−21.22022	19.71	0.57	−0.721	0.308	2.045	0.197	0.151	−5.9	SGB
Pal12-023	326.63146	−21.27247	20.10	0.41	−0.524	0.326	1.815	0.211	0.398	16.7	SGB
Pal12-024	326.63589	−21.27544	20.43	0.39	−0.712	0.373	1.829	0.234	0.251	44.1	MS
Pal12-025	326.65113	−21.27800	20.72	0.36	−0.846	0.395	1.659	0.265	0.154	32.6	MS